This is a repository copy of *Metal-organic framework nanosheets: programmable 2D materials for catalysis, sensing, electronics, and separation applications*.

White Rose Research Online URL for this paper:
https://eprints.whiterose.ac.uk/176700/

Version: Published Version

Check for updates

Metal-Organic Framework Nanosheets: Programmable 2D Materials for Catalysis, Sensing, Electronics, and Separation Applications

Joshua Nicks, Kezia Sasitharan, Ram R. R. Prasad, David J. Ashworth, and Jonathan A. Foster*

Metal-organic framework nanosheets (MONs) have recently emerged as a distinct class of 2D materials with programmable structures that make them useful in diverse applications. In this review, the breadth of applications that have so far been investigated are surveyed, thanks to the distinct combination of properties afforded by MONs. How: 1) The high surface areas and readily accessible active sites of MONs mean they have been exploited for a variety of heterogeneous, photo-, and electro-catalytic applications; 2) their diverse surface chemistry and wide range of optical and electronic responses have been harnessed for the sensing of small molecules, biological molecules, and ions; 3) MONs tunable optoelectronic properties and nanoscopic dimensions have enabled them to be harnessed in light harvesting and emission, energy storage, and other electronic devices; 4) the anisotropic structure and porous nature of MONs mean they have shown great promise in a variety of gas separation and water purification applications; are discussed. The aim is to draw links between the uses of MONs in these different applications in order to highlight the common opportunities and challenges presented by this promising class of nanomaterials.

1. Introduction

Metal-organic framework nanosheets (MONs) have rapidly established themselves as a distinct class of hybrid nanomaterials with a multitude of remarkable properties and potential applications.[1,2] MONs are free standing nanosheets approaching monolayer thickness formed by organic linkers coordinated to metal nodes in two-dimensions.[3] As with other 2D materials, MONs offer advantages over their bulk counterparts in terms of their high external surface areas, nanoscopic dimensions, and anisotropic structures. However, their metal-organic composition

offers advantages over simple inorganic nanosheets in that a diverse range of physical and chemical properties can be programmed into their crystalline structure (**Figure 1**). This distinct combination of properties makes MONs ideal for a wide range of catalysis, sensing, electronics, and separation applications which will be the focus of this review.

Much of the early literature in this field focused on the development of novel MON architectures and new routes towards their synthesis. A diverse range of different metal ions and organic linkers have been used to construct MONs.[4] However the field has rapidly converged on a handful of popular secondary building units (SBUs) which dominate much of the literature thanks to their reliable formation of high aspect ratio nanosheets. Popular classes of MONs that have been widely applied by different groups in applications include those based on the metal paddle-wheel (PW) motif,[5–7] axially capped Zr and Hf clusters,[8–11] 2D zeolitic imidazolate frameworks (ZIFs),[12–14] and square planar Ni, Co, and Cu SBUs.[15–18] The modular structure of MONs, ease of functionalization and diverse range of materials they can be combined with means that MONs can be readily "programmed" to provide the desired topology and properties required for a given application.

A wide variety of methods have been explored to synthesize MONs, either "top-down" by the exfoliation of layered metal-organic frameworks (MOFs) or "bottom-up" by assembly of molecular building blocks directly into nanosheets. The majority of top-down approaches utilize mechanical energy to overcome inter-layer interactions, such as liquid-assisted ultrasonication,[19] shear-mixing,[20] and grinding/ball-milling,[13] or the less common freeze-thaw[21] and "scotch-tape" methods.[22,23] Other methods involving photochemical,[24] electrochemical,[25] and chemical intercalation,[26] have also been developed but are less widely used. Bottom-up methodologies typically utilize surfactants or modulators to inhibit crystal growth in one dimension,[12,27,28] or layering/interfacial methods to promote anisotropic growth.[15,29,30] The use of sacrificial 2D templates has also recently emerged a promising route.[31,32] Each approach has advantages and disadvantages in terms of the thickness, lateral dimensions, size distribution, quantity and quality of the MONs produced, and the best approach therefore varies depending on the application.

J. Nicks, Dr. K. Sasitharan, Dr. R. R. R. Prasad, Dr. D. J. Ashworth,
Dr. J. A. Foster
Department of Chemistry
The University of Sheffield
Brook Hill, Sheffield S3 7HF, USA
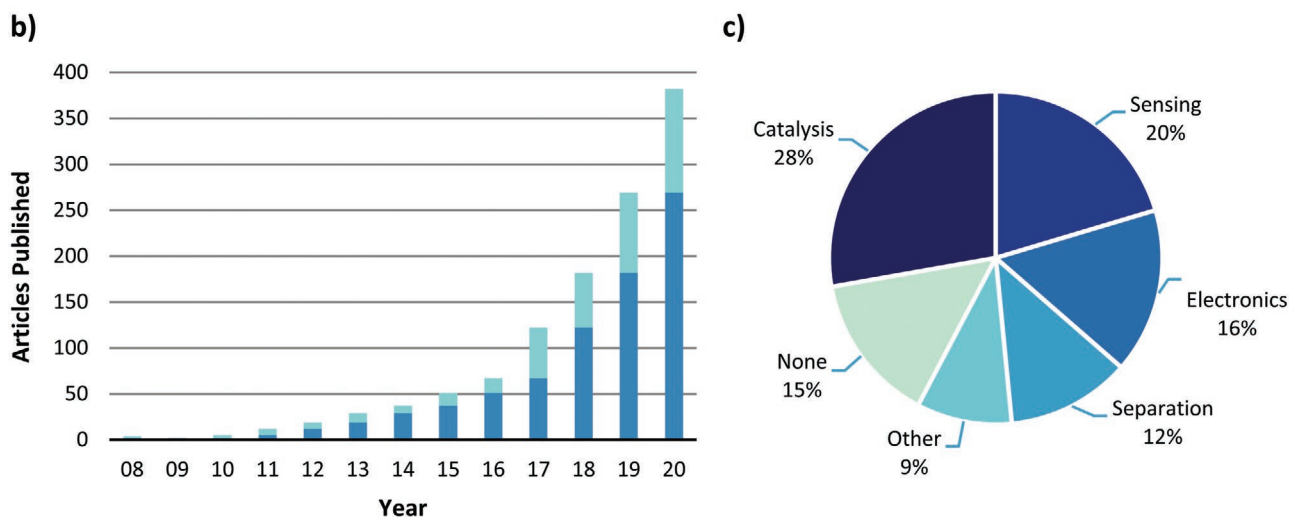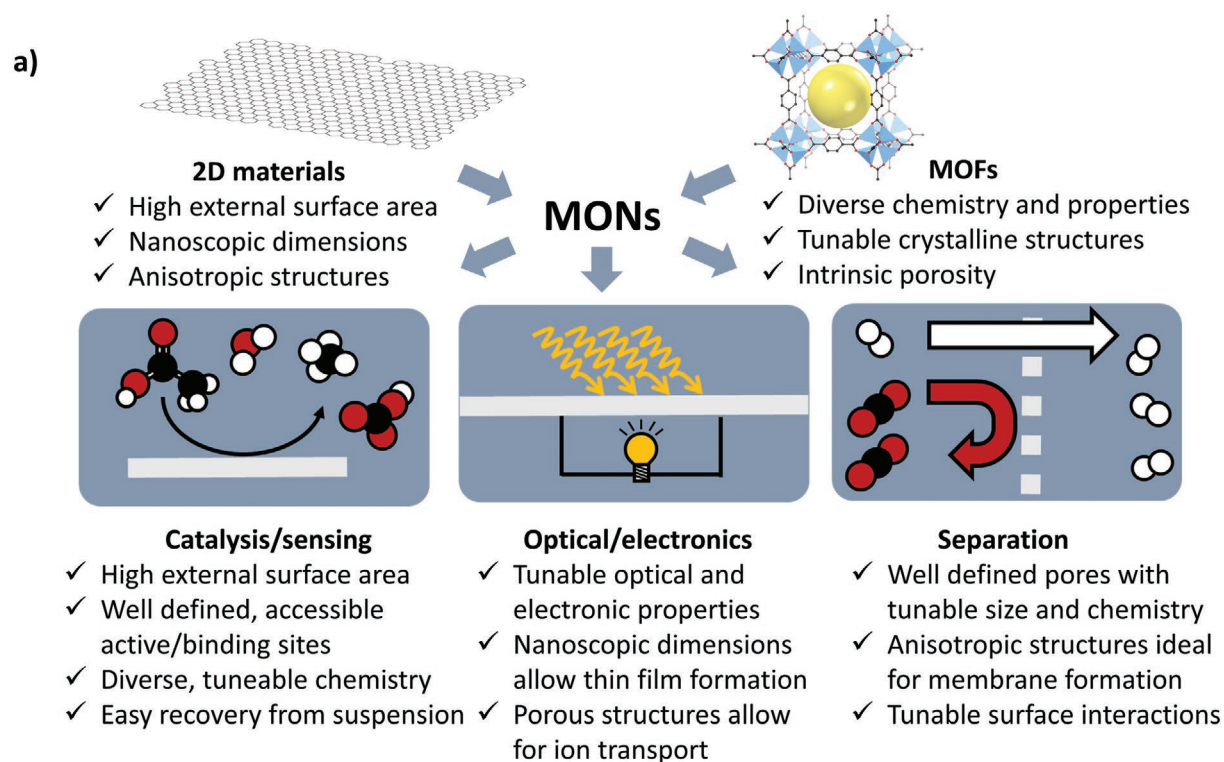E-mail: jona.foster@sheffield.ac.uk

a)

b)

c)

Figure 1. a) Scheme summarizing the key properties of MONs exploited in each application area. b) A chart showing the number of new articles involving MONs published each year (light blue) and the cumulative total of articles published in previous years (dark blue). c) Pie chart showing percentage of articles categorized based on application. Data based on a library of papers which meet our definition of MONs outlined in ref. [2].

These topics and the early literature have been reviewed by both us,[2] and others.[1,33,34] There has also been increasing recognition of MONs in reviews discussing other 2D materials,[35–38] or layered MOFs.[39] However, the field has advanced rapidly in recent years with more than 80% of the 382 papers we are aware of on this topic published since our previous review in 2017 (Figure 1). During this time, the focus has shifted from developing new synthetic methods and novel systems, towards utilizing their distinct properties in different applications.[40–43] This trend is reflected in many of the more recent reviews, which have focused on the use of MONs within

a single specific application, including: functional devices,[40] gas separation,[43] membrane separation,[41] and electrocatalysis.[44] To give an indication of the extent of literature on MONs in each application, within our curated library of MON papers, the pie charts shown in Figure 1c highlight the percentage of papers demonstrating the various emerging applications of MONs. MONs possess the high-surface area, nanoscopic dimensions and anisotropic structures of 2D materials, as well as, the diverse chemistry, tuneable periodic structures, and intrinsic porosity of their bulk counterparts, MOFs. Different combinations of these features intuitively make them relevant

**ADVANCED
SCIENCE NEWS**

www.advancedsciencenews.com

**ADVANCED
FUNCTIONAL
MATERIALS**

www.afm-journal.de

for a wide range of different applications as summarized in Figure 1a.

In this review, we aim to bring together the current literature on the use of MONs in four diverse application areas. Following this introduction (Section 1), the review is split into sections based on the broad application areas of 2) catalysis, 3) sensing, 4) electronics, and 5) separation. The opening to each section provides a brief overview of the potential of MONs within this broad application area and the section is then organized by more specific applications. Our focus is on examining the underlying role of the MONs within each application and identifying examples where MONs have been able to outperform other 2D materials and metal-organic materials. Examples have been chosen to highlight the range of roles that the MONs can play within each application, as well as, to highlight particularly interesting or high performing systems. A perspective on the current literature for each application is offered at the end of each section whilst the final section 6) offers our overall perspective on the future opportunities and challenges for translating MONs into real-world applications. Our ambition is that by providing a holistic overview of the different ways MONs have been harnessed, the reader will gain inspiration from ideas, techniques, and materials used in one application to develop their own research in another area.

2. Exposed Active Sites for Catalysis

New catalysts are needed to reduce the cost and energy required to synthesize existing compounds, access new drugs and pesticides, split water, and capture carbon from the atmosphere. MONs combines many of the desirable aspects of homogeneous and heterogeneous catalysts in having well defined, tunable active sites but also allowing easy recovery from the reaction mixture or immobilization on supports or as thin films. A key limitation of 3D MOFs as catalysts is that their active sites are typically buried within the bulk of the framework which can limit the rate at which reagents and products can interact with them. In contrast, the high external surface area of MONs means their active sites are directly exposed to solution potentially leading to enhanced rates of catalysis compared to their 3D counterparts. MONs can be formed using a diverse range of metal-ions and ligands which can either be inherently catalytic themselves, or further functionalized with catalytic species. Multiple functionalities can also be brought together to create sophisticated catalysts to imbue selectivity or enable multistep cascade reactions. In the following section we discuss how MONs have so far been used for heterogeneous-, photo- and electro-catalysis and highlight the different approaches and reactions that have been investigated in each case.

2.1. Heterogeneous Catalysis

2.1.1. Metal-Sites

Coordinatively unsaturated metal-sites present in the metal-clusters of MONs can act as Lewis acidic sites capable of promoting organic reactions. These active sites are usually generated via the removal of cluster coordinated solvent molecules after the MON synthesis. MONs based on the PW SBUs were some of the earliest examples of MON-based Lewis acidic catalysts. Fu and co-workers employed CoBDC (BDC = 1,4-benzene dicarboxylate) MONs with unsaturated Co^{2+} metal-sites in the cycloaddition of CO_2 with styrene epoxide.[45] They observed higher conversion and greater selectivity towards styrene carbonate compared to the bulk MOF. The CuBDC and NiBDC analogues have also been reported and shown to out-perform their bulk counterparts when catalyzing a variety of other reactions. CuBDC MONs catalyzed the aerobic oxidation of benzyl alcohols and epoxidation of cyclic and linear olefins (**Figure 2**a).[46,47] NiBDC MONs were used to promote the Knoevenagel condensation between propane dinitrile with various aromatic, as well as, aliphatic aldehydes.[48] Ultrathin NiBDC MONs on graphene oxide or graphitic carbon nitride composite materials also exhibited higher hydrogenation activity than the corresponding MOF-composite materials in the reduction of organic water pollutant 4-nitrophenol (4-NP) to the industrially useful precursor 4-aminophenol (4-AP) in H_2 atmosphere.[49] Surfactant-assisted synthesis of known MONs have been reported by multiple groups as a method to generate more accessible metal-sites via tuning their thickness and porosity. Polyvinylpyrrolidone (PVP) mediated CuTCPP (TCPP = Tetrakis(4-carboxyphenyl)porphyrin) synthesis yielded ultrathin MONs exhibiting higher efficiency and selectivity in styrene oxidation than bulk CuTCPP synthesized without PVP (Figure 2b).[50] Mesoporous CuBDC MONs obtained by cetyltrimethylammonium bromide (CTAB) assisted synthesis showed higher conversion in C-S coupling of bulk substituents than the microporous MOF.[51]

More recently MONs based on the more robust and Lewis acidic Zr and Hf clusters have been reported. 2D architectures were achieved by restricting the connectivity of the cluster to a plane via the addition of large amount of modulator (usually monocarboxylic acids) molecules. The cluster defects arising from this "restricted synthesis" can result in the formation of coordinatively unsaturated Zr or Hf sites promoting catalysis. The Zhao group reported that nanosheets obtained by the exfoliation of hxl-UiO-67 synthesized using this approach showed higher degrees of conversion in the cyanosilyation of aromatic aldehydes than the bulk MOF (Figure 2c).[52] Similarly, NUS-8(Zr) MONs obtained using modulator assisted synthesis that produced a high density of active sites facilitated the selective oxidation of thioethers (Figure 2d).[8] NUS-8(Zr) MONs showed >99% conversion and 100% selectivity towards sulfones at room temperature. In comparison to its 3D interpenetrated analogue, NUS-8(Zr) MONs exhibited higher reaction kinetics owing to their 2D structure enabling faster access across the active sites.

Ultrasonic exfoliation methods often used for MONs synthesis from bulk MOF systems can generate coordinatively unsaturated metal-sites due to the linker vacancies created during the procedure. Recently, Cheng and co-workers employed this method to produce ultrathin Ni-based MONs for ethylene dimerization.[53] The Ni-MONs promoted ethylene dimerization with a turnover frequency (TOF) of 5536 h^{-1} and 75.6% selectivity towards 1-butene at 25 °C in the presence of alkylaluminium cocatalyst, Et_2AlCl. This activity was found to be twice of that shown by the bulk Ni-MOF with saturated

**ADVANCED
SCIENCE NEWS**

www.advancedsciencenews.com

**ADVANCED
FUNCTIONAL
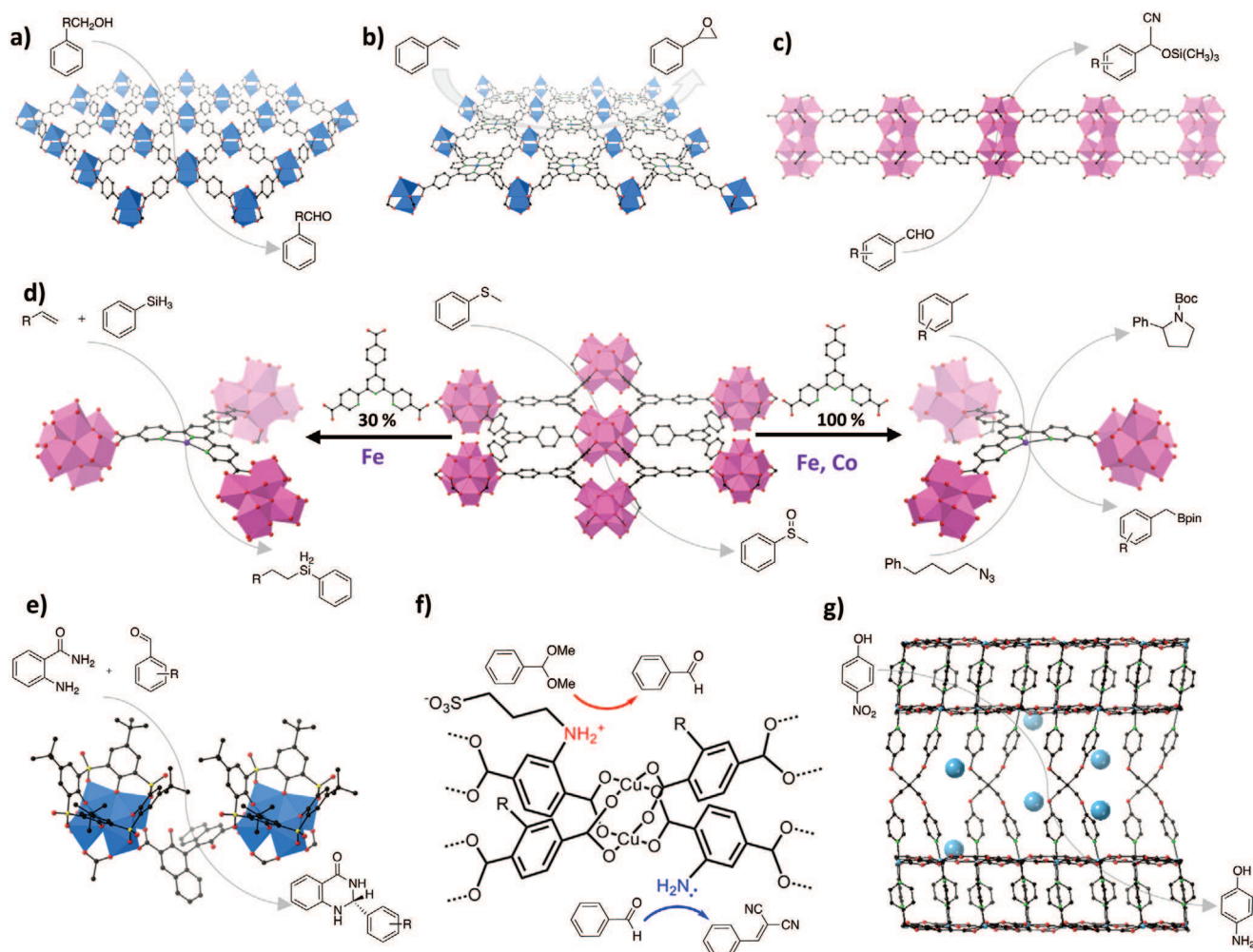MATERIALS**

www.afm-journal.de

Figure 2. Various heterogeneous catalytic reactions promoted by different MONs: a) CuBDC catalyzed aerobic oxidation of benzyl alcohols, b) CuTCPP catalyzed styrene oxidation, c) UiO-67 MON catalyzed cyanosilylation of aromatic aldehydes, d) Reactions promoted by Zr/Hf-BTB MON and its isoreticular derivatives: (Middle) Coordinatively unsaturated Zr/Hf sites catalyzed selective oxidation of thioanisole, (left) hydrosilylation of terminal olefins catalyzed by Hf-BTB MON with 30% TPY loading post-metalated with Fe and (right) Hf-TPY MONs after post-metalation with Co and Fe catalyzed C—H borylation of methylarenes and intramolecular C_{sp}^3—H amination of alkyl azides, e) enantioselective 2,3-dihydroquinazolinones synthesis catalyzed by 1,1'-binaphthol moieties of Zn MON, f) post-synthetically functionalized CuABDC catalyzed tandem Knoevenagel condensation of benzaldehyde dimethyl acetal to benzylidene malononitrile, and g) Ni/MOF-Ni-0.4 catalyzed 4-NP to 4-AP reduction.

metal centers. AFM imaging of the MONs showed the thickness of nanosheets decreases in each catalytic run, implying further in situ exfoliation during catalysis. Further analysis proved that, although Ni leaching is accompanied in each exfoliation step, in situ generation of new active sites in a "snake's moulting" manner helped the catalyst to maintain its activity.

Another strategy that has been used to design MON catalysts for specific reactions is to incorporate metalloligands or organo-catalysts known to be active under homogeneous conditions into the MON scaffold. The seminal works in this area was reported by the Lin group using Hf-BTB (BTB = benzene tribenzoate) MONs and its isoreticular derivatives (Figure 2). Hf-BTB MONs incorporated with 30% 4'-(4-benzoate-2,2',2''-terpyridine)-5,5''-dicarboxylate (TPY) linkers after post-metalation with FeBr$_2$ afforded Fe-TPY-MON precatalysts for the hydrosilylation of terminal olefins (Figure 2d).[27] After activation using NaBHEt$_3$, Fe-TPY-MON catalyzed complete hydrosilylation of styrene with

a turnover number (TON) > 5000 and 100% selectivity towards the anti-Markovnikov product. In contrast, the homogeneous catalyst (Fe-TPY) formed the Markovnikov product with significantly lower yields (30%). References run using the bulk layered MOF produced 30% yield whilst no detectable product was observed for the 3D interpenetrated MOF also used as a control.

In a concurrent study, Hf-TPY MONs after post-metalation with Co and Fe were activated with NaBHEt$_3$ to generate MON stabilized M^{II}-(TPY$^·$)$^{2-}$ active catalysts.[10] Activated CoCl$_2$.TPY-MON catalyzed the C—H borylation of *m*-xylene in the presence of bis(pinacolato)diboron, to afford borylated products in high yields (95%) with selectivity towards benzylic position (5.7:1) (Figure 2d). Similarly, FeBr$_2$.TPY-MON catalyzed intramolecular C_{sp}^3—H amination of 1-azido-4-phenylbutane to give Boc-protected α-phenyl pyrrolidine in the presence of di-*tert*-butyl dicarbonate in good yield (Figure 2d). The homogeneous

analogues, CoCl$_2$.TPY and FeBr$_2$.TPY showed only negligible conversion due to catalyst disproportionation into nanoparticles under reaction conditions. This is an interesting example of MONs used to stabilize reactive sites. In a recent study, using 2-chloro-1,10-phenanthroline as the co-ligand, active Pd^{2+} center was incorporated to the Hf-TPY MONs by Chang and co-workers.[54] After treating with Selectfluor/H$_2$O, the active species, (N-fluoroxy)-(2-chloro)-phenanthrolinium, formed acts as a stoichiometric solid fluorination agent with varying regioselectivities and conversions comparable to homogeneous analogues.

2.1.2. Organic Ligands

In addition to catalysis taking place at post-synthetically coordinated metal-sites, functional groups of organic linkers on the MON surface can also promote catalytic reactions. In a pioneering contribution, Cui and co-workers showed how adding chiral organocatalytic groups to MONs can impart enantioselectivity to otherwise non-enantioselective organocatalysts.[55] They combined 1,1′-binaphthol/-biphenol dicarboxylic acids with zinc clusters to create layered MOFs which were then exfoliated to form the corresponding MONs. The resulting nanosheets were used for the asymmetric cascade reaction of aminobenzamide and aldehydes to produce 2,3-dihydroquinazolinones (Figure 2e). The MONs showed higher yields (56–90% for MOFs and 72–94% for MONs) and a higher ee (46–72% for MOFs and 64–82% for MONs) than the corresponding MOFs whilst the homogeneous linker exhibited no enantioselectivity.

In our own work we showed that covalent post-synthetic functionalization can be used to enhance the exfoliation of layered MOFs and add organic catalytic functionalities.[56] Layered Cu(ABDC) MOFs (ABDC = 2-amino benzenedicarboxylate) were partially functionalized (up to 25%) with 1,3-propanesultone and then exfoliated using ultrasound. The resulting nanosheets possessed both acidic and basic sites which enabled them to promote the one-pot, two-step tandem Knoevenagel condensation of benzaldehyde dimethyl acetal to benzylidene malononitrile in high yields (Figure 2f). Whilst the MONs showed 82% conversion towards desired benzylidene malononitrile, less than 5 % conversion was observed for the unexfoliated MOFs and unfunctionalized MONs. The MONs were also recovered from suspension and reused producing 86% yield.

2.1.3. Immobilized Species

In addition to functionalization with metal-ions and organic groups, another promising approach is to immobilize metal nanoparticles (MNPs) onto the surface of MONs.[57–59]

One of the most widely investigated reactions promoted by immobilized species is 4-NP to 4-AP reduction. The earliest example of this reaction was reported by Lu and co-workers who deposited AuNPs on a mixed-linker Ni MON to form Au-1@Ni-MON.[57] The MONs prevented aggregation of the AuNPs enabling efficient conversion of the 4-NP to 4-AP with a rate constant of 4.4×10^{-1} min^{-1}. Longer reaction times were observed for the reduction of a larger dye, Mordant green, indicating a size selectivity not observed in control studies using

pure AuNPs. In a similar study, the Zeng group deposited mono-, bi- and trimetallic MNPs onto Cu(HBTC)-MONs (BTC = 1,3,5-benzene tricarboxylate).[58] Among all the tested catalysts, Au$_{0.3}$Pt$_{0.3}$Pd$_{0.4}$ was found to be the most highly active with a rate constant of 0.478 min^{-1} for the conversion of 4-NP to 4-AP due to the synergistic activity of the MNPs. CuTCPP MONs with immobilized AuNPs generated via in situ hydrothermal growth showed nearly threefold enhancement (0.200 min^{-1}) in their activity for 4-NP to 4-AP reduction when compared to pure AuNPs (0.082 min^{-1}).[59] Ferrocenedicarboxylate (FDC) based Zr MONs decorated with AuNPs were also shown to catalyze the 4-NP to 4-AP reduction efficiently.[60] Recently, NiNPs deposited on Ni/NMOF-Ni-0.4 nanosheets obtained by the partial reduction of NMOF-Ni nanosheets catalyzed the 4-NP to 4-AP reduction with high efficiency than the unfunctionalized MON (Figure 2g).[61] The non-noble MNPs-MON composite showed a rate constant 7.92×10^{-3} s^{-1} and the authors suggested this could be an economically viable replacement to noble MNPs based catalysts.

Recently, the Han group deposited ultra-small RuNPs onto UiO-66 MONs synthesized using a bio-based surfactant-assisted method and investigated their use for the hydrogenation of levulinic acid to valerolactone.[62] The sub-2 nm RuNPs showed 10 times (349 h^{-1}) more activity when supported on the MONs than on the bulk UiO-66 (38 h^{-1}). The higher activity of MONs was attributed to the ease of accessing well-dispersed RuNPs on the MON surface than those confined within MOF pores. PdNPs loaded FDC-based Zr MONs obtained via in situ reduction of K$_2$PdCl$_4$ reported by Shea and co-workers showed very-high catalytic activity in styrene hydrogenation with a TOF of 7968 h^{-1} in comparison to the bulk Pd@UiO-66 (271 h^{-1}).[63] Furthermore, the Wang group recently showed how MONs can drastically improve the selectivity of PtNPs by even distribution of the latter on its surface. While Zr-2,2′-bipyridine-5,5′-dicarboxylate (ZrBPyDC) MONs exclusively yielded cinnamyl alcohol from cinnamaldehyde via transfer hydrogenation with NH$_3$BH$_3$, PtNPs alone produced a mixture of cinnamyl alcohol and phenyl propanol. In striking contrast to this, Pt@ZrBPyDC and NH$_3$BH$_3$ selectively formed phenyl propanol through a combination of transfer and catalytic hydrogenation reactions.[64] The reaction without any high-pressure hydrogen source was applicable to a range of α,β-unsaturated alcohols.

In an interesting study, Tan and co-workers reported the influence of MON structure in dictating the active Pd species formed.[65] The OX-1 MONs with (Et$_3$NH)$_2$Zn$_3$BDC repeating units favors the formation of atomic and small cluster Pd species that selectively resides on the benzene rings of the BDC linking units. The resulting Pd@OX-1 showed excellent catalytic activity in Suzuki coupling and Heck arylation under various reaction conditions. Pd@OX-1 shows the unique property of recapturing the active Pd species during the reaction, hence enabling the catalyst recycling.

2.2. Photocatalysis

2.2.1. Porphyrin-Based Metal-Organic Framework Nanosheets

Porphyrins are nature's light harvesters and M-TCPP have been widely used as a linker within MONs thanks to their planar
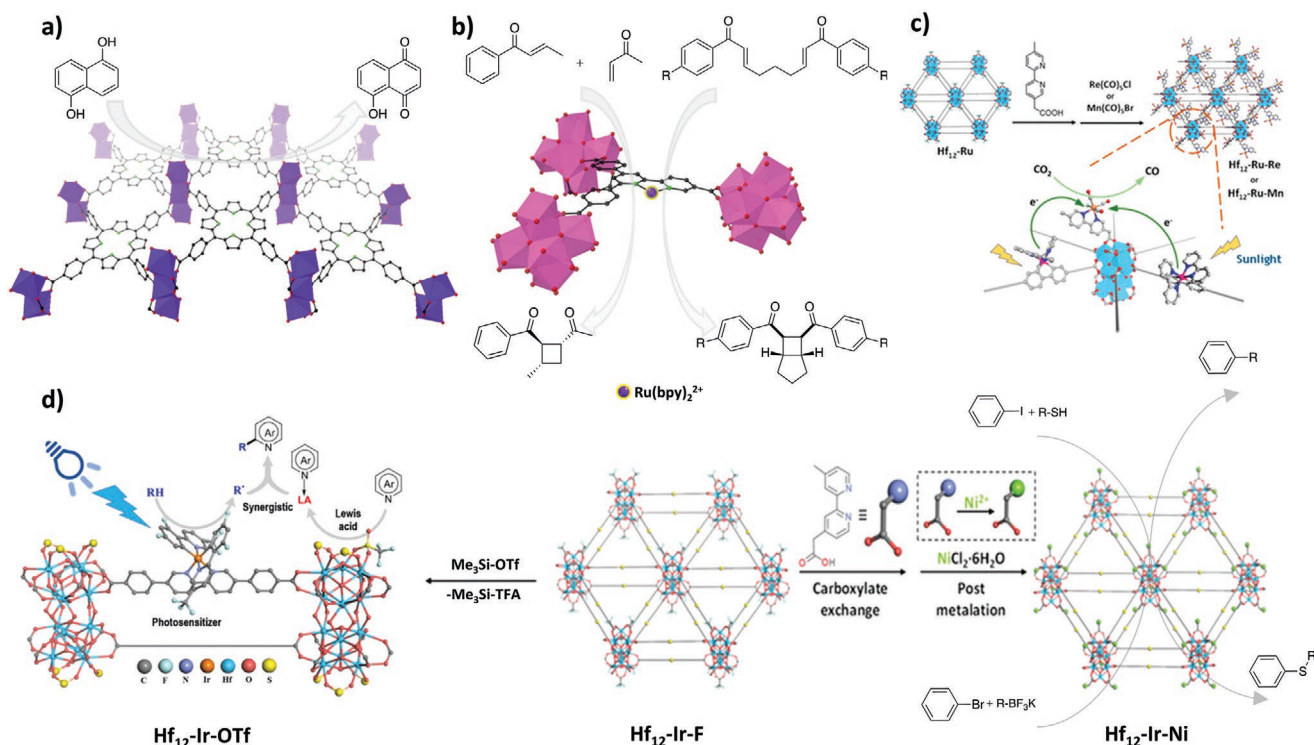
ADVANCED
SCIENCE NEWS
www.advancedsciencenews.com

ADVANCED
FUNCTIONAL
MATERIALS
www.afm-journal.de

Figure 3. a) Ln MONs catalyzed photocatalytic conversion of 1,5-dihydroxynaphthalene to juglone. b) Zr-RuBPY MON catalyzed crossed [2+2] cycload-ditions of acyclic enones and intramolecular cycloaddition of bisenones. c) Schematic representation of post-synthetic modification of Hf$_{12}$-Ru to access Hf$_{12}$-Ru-Re/Mn and Hf$_{12}$-Ru-Re mediated photocatalytic reduction of CO$_2$. Reproduced with permission.[72] Copyright 2018, American Chemical Society. d) (Middle) Schematic representation of post-synthetic modification of Hf$_{12}$-Ir-F to Hf$_{12}$-Ir-OTf and Hf$_{12}$-Ir-Ni, (Left) Hf$_{12}$-Ir-OTf catalyzed Minisci-type cross-coupling reactions of heteroarenes and (Right) Hf$_{12}$-Ir-Ni catalyzed C—S and C—C coupling reactions. Reproduced with permission.[74] Copyright 2019, American Chemical Society. Reproduced with permission.[75] Copyright 2020, American Chemical Society.

structure and high connectivity. M-TCPP MONs (M = Pd, Ni) have been used to promote photocatalytic oxidation of 1,5-dihydroxynapthalene (DHN) to juglone upon visible light irradiation.[26,66] Enhanced photocatalytic activity for DHN to juglone was recently reported for mixed-metal Ln MONs with TCPP linkers (**Figure 3a**).[67] The improved efficacy of the catalyst here is attributed to the energy and electron transfer between the linker and Yb^{3+} based metal-clusters. TCPP has also been added to Zr-BTB MONs to form ultrathin PCN-134 MONs by Zhou and co-workers.[68] The distance between the adjacent metal-clusters in Zr-BTB MONs matches the distance between the carboxylate groups of the TCPP linker enabling the functionalization of PCN-134 MONs. This system was found to be stable under adverse chemical conditions without any significant leaching problems compared to other porphyrin linkers employed. Moreover, under visible light irradiation, PCN-134(Ni) (NiTCPP functionalized) catalyzed the conversion of dihydroartemisinic acid to artemisinin in 64% yield. The catalyst was found to be significantly more active than its layer-pillar-type 3D analogue with limited accessibility to catalytic centers.

2.2.2. Post-Synthetic Modification of Zr/Hf-Based Metal-Organic Framework Nanosheets

Several exciting examples showing how post-synthetic modification can be used to create sophisticated photocatalysts have

been provided by Lin and co-workers. Hf-TPY MONs after post-metalation with FeBr$_2$ were examined in the photocatalytic oxidation of THF.[69] The hydrophilic-hydrophobic nature of the MONs were "tailored" via post-synthetic functionalization of the metal-clusters with various monocarboxylic acids prior to metalation. The functionalized Fe-TPY-MONs showed varying selectivity towards butyrolactone (BTL) and 2-hydroxytetrahydrofuran in the photocatalytic oxidation of tetrahydrofuran (under blue LED irradiation). However, the highly hydrophilic gluconic acid functionalized GA-Fe-TPY-MON showed 100% selectivity towards BTL, with a TON of $5.3 \pm 0.3 \times 10^2$ under identical reaction conditions. The enhanced catalytic activity of GA-Fe-TPY-MON was attributed to the optimal residence time of the reactive intermediates in the high hydrophilic MON environments.

The Lin group have also shown how the bipyridine sites of isoreticular Zr-4′6′-bis(4-benzoate-)2,2′-bipyridine)-5-carboxylate (Zr-BPY) can be post-metalated with Ru(bpy)$_2$Cl[2] to afford Zr-RuBPY MON photocatalyst (Figure 3b).[70] While Zr-RuBPY MON promoted the [2+2] intramolecular cycloaddition of bisenone upon irradiation with a blue LED (460 nm) to yielded mesodiastereomer of cyclobutene bicyclic dione in good yield, the reference UiO-67 MOF with Ru(bpy)$_3$ functionality exhibited only negligible conversion. Similar activities were observed for crossed [2+2] cycloadditions of acyclic enones and Meerwein reactions. In contrast to this, both MON and MOF showed very similar activity in the reductive cyclization

of bis(enones), which was attributed to the ease of accessing catalytic centers in the octahedral pores via tetrahedral pores of the MOF without any restrictions. This is a rare example in which both the MOF and MON exhibit the similar activity for a specific reaction. Upon examining the pore architecture of the MOF, the Ru(bpy)₃ functionality was found to be occupying the octahedral pores allowing the bis(enones) substrates to reach the active sites through tetrahedral pores without any interference, explaining the similar activity. Photopolymerization has also been catalyzed by isoreticular Hf-IrBPY MONs, obtained via post-metalation of Hf-BPY MONs with Ir₂(ppy)₄Cl₂. The MONs catalyzed the atom-transfer radical polymerization of methyl methacrylate to afford poly(methyl methacrylate) following irradiation with a blue LED (410 nm) in the presence of α-bromophenylacetate as a co-initiator.[71] The corresponding MOF failed to photopolymerize and exhibited low catalytic efficiency under identical conditions.

In the photocatalytic hydrogen evolution reaction (HER), Hf_{12} cluster based UiO-67 MONs showed an 84-fold increase in photocatalytic efficiency than the bulk UiO-67. Furthermore, upon post-synthetic modification of clusters with Ti^{4+}, the activity again increased by a factor of 13 under same reaction conditions.[52] Remarkably sophisticated photocatalysts have also been created by Lin and co-workers using MONs consisting of Hf_{12} clusters bridged by dicarboxylic acid linkers. In one example, MONs formed using bis(2,2'-bipyridine)[5,5'-di(4-carboxyl-phenyl)-2,2' bipyridine]ruthenium (II) dichloride linkers were further functionalized via post-metalation of the monodentate bipyridyl linkers incorporated on the Hf_{12} clusters via modulator exchange with $Re(CO)_5Cl/Mn(CO)_5Br$ clusters (Figure 3c).[72] This arrangement meant that each Re or Mn catalytic site was held in close proximity to six Ru-functionalised linkers, enabling multi-electron transfer which facilitated the photocatalytic reduction of CO_2. In contrast to other post-synthetically functionalized Zr/Hf systems,[73] Hf_{12}-Ru-Re MONs showed unprecedented efficiency with TON ≈670 in 6 h under sunlight irradiation and a cumulative TON of 8613 under artificial visible light.

Using similar synthetic strategy, an isoreticular Hf_{12}-Ir-F MON with Ir functionalized dicarboxylate linkers (Ir(DBB) [df(CF₃)ppy]₂⁺ where DBB = 4,4'-di(4-benzoato)-2,2'-bipyridine, df(CF₃)ppy = 2,-(2,4-difluorophenyl)-5-(trifluoromethyl)pyridine referred as DBB-Ir-F), were post-metalated with $NiCl_2.6H_2O$ to afford Hf_{12}-Ir-Ni MONs (Figure 3d).[74] In confined MON environment, upon irradiation with blue light (410–480 nm), the enhanced electron transfer from photoexcited DBB-Ir-F to Ni sites facilitated various photocatalytic reactions involving single-electron transfer to afford C−S, C−O, and C−C coupling products in excellent yields and high TONs. In a concurrent study based on the same system, trifluoroacetate groups in the metal-clusters were replaced with triflate (OTf) groups via metathesis reaction using trimethylsilyltriflate, to generate Hf_{12}-Ir-OTf with highly Lewis acidic metal-clusters (Figure 3d).[75] Hf_{12}-Ir-OTf MONs with Lewis acidic and photoredox centers working in synergy gave excellent to moderate yields (93–46%) with high TON (950–580) in the Minisci-type cross-coupling reactions of heteroarenes with ethers, amines and unactivated alkenes.

Solar fuels generated via photocatalysis are considered promising as a method for energy generation. MONs have the potential to play a role in the light absorption, charge funneling and redox reactions as part of these systems.[76] Qiao et al. used a 2D Ni-based MOF (NMF) $[Ni(phen)(oba)]_n \cdot 0.5nH_2O$ (phen = 1,10-phenanthroline, oba = 4,4'-oxybis(benzoate)), as a platform to host cadmium sulphide (CdS) photocatalyst resulting in the best performing example (highest activity) of a noble-metal free photocatalytic H_2 generation of this kind (**Figure 4**a).[77] The authors demonstrated the formation of a staggering-type heterojunction between the MONs and CdS. Upon visible-light illumination, the photo-induced electrons transfer from the conduction band of CdS and migrate to active centers on the surface of the MONs that reduce protons to generate H_2 gas. The photo-induced holes remain on the valence band of CdS for the oxidation of lactic acid.

Duan et al. demonstrated the loading of plasmonic AuNPs on Co-PPF3 MONs (CoTCPP with bipyridine pillars prepared by surfactant-assisted method) for photocatalytic CO_2 generation.[78] The authors showed that the hot electrons generated by surface plasmon resonance excitation of the NPs have higher fermi levels and can easily be injected into the Co^{2+} centres of the MON leading to a higher photocatalytic efficiency. The plasmon resonance energy transfer effect was found to become weaker with increasing thickness of the MONs. Efficient photoelectrochemical reduction of CO_2 was demonstrated by Sun and co-workers using ZnTCPP MONs as semiconducting photosensitizers along with ZIF-67 as co-catalyst (Figure 4b).[79] Photoelectrochemical impedance measurements from the fabricated device and steady state PL measurements showed that MONs enabled better charge transport, efficient separation and longer lifetime of the photogenerated charge-carriers.

In all the previously described examples, the hybrid catalysts are assembled via physical/electrostatic interactions. Liu et al. show that the attachment of carbon nitride quantum dots (g-CNQDs) via coordination to the Co active sites in CoTCPP based photosensitizer improves directional transfer of the photogenerated electrons from the quantum dots to the Co sites for efficient photocatalytic reduction of CO_2 (Figure 4c).[80] The low dimensionality of both the components enabled spatial separation of the photoexcited charge carriers and acceleration of charge transfer.

2.3. Electrocatalysis

2.3.1. Oxygen Evolution Reaction

The oxygen evolution reaction (OER) is a two-step, four-electron transfer process which finds a wide range of applications in energy storage and conversion devices such as metal-air batteries and solar cells. Qiao and co-workers demonstrated the use of MONs to enhance the electrocatalytic behavior of $Ni(OH)_2$ nanosheets in OER.[81] Although $Ni(OH)_2$ nanosheets by themselves exhibit intrinsic water oxidation ability, high stability, and corrosion resistance, the low-oxidation state of Ni reduces its electrocatalytic activity. To address this drawback, a NiBDC/$Ni(OH)_2$ hybrid material was synthesized via sonication assisted growth of NiBDC MONs on $Ni(OH)_2$ nanosheets (Figure 4d). Co-ordination of BDC to the Ni sites on the $Ni(OH)_2$ nanosheets reduces the electron density around Ni atoms in

**ADVANCED
SCIENCE NEWS**

www.advancedsciencenews.com

**ADVANCED
FUNCTIONAL
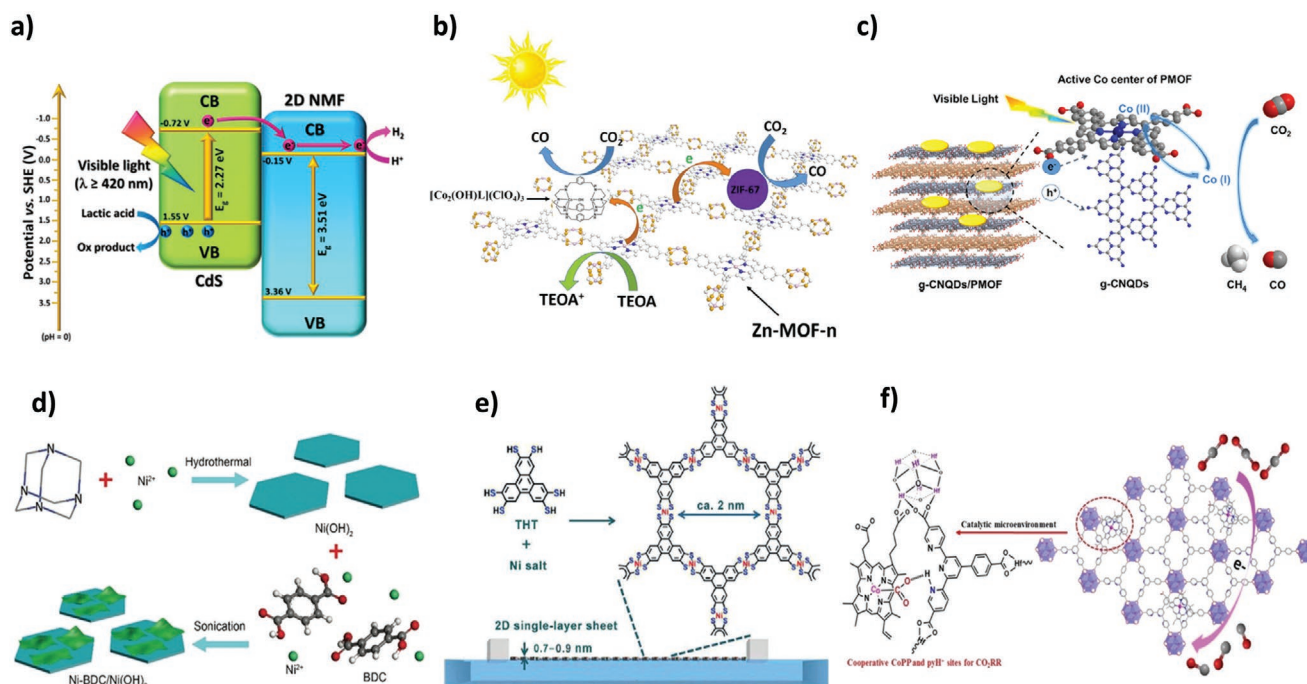MATERIALS**

www.afm-journal.de

Figure 4. a) The excitons dissociation and transfer in the 2D NMF/CdS heterostructure under visible-light irradiation. The pink and blue spheres denote photoinduced electrons and holes, respectively. Reproduced with permission.[77] Copyright 2019, Wiley. b) A MON/complex or MON/ZIF system for CO_2 photoreduction with Zn-MOF nanosheets as the photosensitizer. Reproduced with permission.[79] Copyright 2018, Elsevier. c) Proposed mechanism for photocatalysis promoted by g-CNQDs/CoTCPP system. Reproduced with permission.[80] Copyright 2019, American Chemical Society. d) Schematic illustration of NiBDC/Ni(OH)$_2$ heterostructure on Ni(OH)$_2$ nanosheets. Reproduced with permission of the Royal Society of Chemistry.[81] e) Schematic showing the synthesis of Ni-THT MON by Langmuir–Blodgett method. Reproduced with permission.[97] Copyright 2015, Wiley. f) Schematic showing the cooperative action of multiple active-sites in CO_2RR. Reproduced with permission.[103] Copyright 2019, American Chemical Society.

Ni(OH)$_2$, increasing the oxidation state of Ni and so boosting the intrinsic activity of each site. Furthermore, the hybrid structure reduces the aggregation, increasing the number of exposed active sites whilst the porosity of the MONs enables rapid transport of electrolytes to the reaction site and the release of O_2 products. The combination of the effects results in the hybrid materials outperforming NiBDC (5.5 times), Ni(OH)$_2$ (20.6 times), and the benchmark commercial catalysts Ir/C (3.0 times).

MONs have also been used in combination with electrochemically active MNPs in order to enhance OER activity. He and co-workers recently reported the controlled calcination of Ni-MONs for the in situ generation of NiO NPs deposited MONs showing enhanced OER.[82] These NiO/Ni MONs demonstrated low overpotential and Tafel slope values in comparison with parent Ni-MONs and Ni-MONs calcined at 400 °C. The addition of NPs to lamellar MOFs has also been shown to enhance their exfoliation to generate efficient OER catalysts. Zhou and co-workers[83] showed that [Co$_2$(bim)$_4$] (bim = benzimidazolate) embedded with CoFeO$_X$ NPs weakened interlayer interactions resulting in ultrathin MONs in contrast to the layered MOFs without NPs. The CoFeO$_X$ NPs was proposed to consist of coordinatively saturated FeO$_6$ octahedral core with coordinatively unsaturated FeO$_5$/CoO$_5$ edges and highly active interfacial CoO$_2$N$_2$ sites for OER as predicted by theoretical calculations. The nanosheets coated on a carbon cloth showed higher current densities, lower over potentials and faster reaction kinetics than a range of reference samples. Post-catalysis

PXRD indicated retention of crystallinity for the MONs even after 1000 cycles indicating good stability.

In comparison with MONs based on single metals, enhanced OER activity are observed for bimetal MONs.[31,32,84–96] While direct synthesis of bimetal MON systems involves simultaneous use of different metal precursors or metal-doping, layered double hydroxides can also be used as starting materials. The improved intrinsic activity generated by the incorporation of the bimetallic sites in periodic arrangement was attributed to the enhancement OER activity in bimetal MONs. Tang and co-workers reported that Ni and Co-MONs showed high overpotential values of 321 and 371 mV, respectively.[90] Combining both metal centres to create bimetallic NiCo-MONs significantly reduced the over potential to 250 mV. Liu and co-workers showed similar enhancements in OER activity and reduction in overpotential for bimetal MONs based on NiCo and NiFe metalclusters as well.[31] Their NiCoBDC arrays showed an overpotential of 230 mV compared with overpotential values of 308 and 289 mV for references using NiCo powder on layered double hydroxide nanosheets or NiCoBDC powder.

2.3.2. Hydrogen Evolution Reaction

HER is one of the most important reactions from an electrochemical perspective. In addition of being one of the simplest routes to access high purity hydrogen which is utilized as an energy carrier and fuel in electrochemical devices, it is other

**ADVANCED
SCIENCE NEWS**
www.advancedsciencenews.com

**ADVANCED
FUNCTIONAL
MATERIALS**
www.afm-journal.de

half of water-splitting reaction together with OER. MONs based on MN_4, MS_4, and MS_2N_2 (M = Co, Ni) complexes have been recently examined for their electrocatalytic HER activity.[17,97,98] Generally, MONs of monolayer thickness possessing MN_4, MS_4, and MS_2N_2 complexes are obtained by the reaction of appropriate metal precursors with 2,3,6,7,10,11-triphenylenehexathiol or 2,3,6,7,10,11-triphenylhexamine linkers via interfacial synthesis methods (Figure 4e). The mixed-linker MS_2N_2 complex based MONs were found to be more active in comparison with those bearing MN_4 and MS_4 complexes. The higher activity was attributed to the easy accessibility to active sites. Furthermore, DFT studies revealed a protonation step preferentially occurs in the M-N sites of MS_2N_n complex of MONs.

In a recent study, Lin group reported Ce-BTB MONs with Ir and Ru photosensitizers post-synthetically anchored on the metal-clusters for photocatalytic HER.[99] Under visible light irradiation, the photosensitizers and Ce metal-clusters in close proximity promotes HER with high TONs, ≈ 8.7–9.3 times higher than the corresponding homogeneous analogues. Detailed characterization studies revealed a dual photoexcitation pathway where the photoreduced Ir and Ru photosensitizers facilitates the reduction of Ce^{IV} to Ce^{III}, which again on photoexcitation enables the HER. Under acidic conditions, Pt is the ideal electrocatalyst for HER. However, in alkaline condition, the sluggish dissociation kinetics arising from weak $OH^.$ absorption reduces its performance drastically. Sun and co-workers showed that the incorporation of Pt NPs on MON surfaces can impart HER activity to otherwise electrochemically inert Ni-MONs in both acidic and alkaline media.[100]

2.3.3. Carbon Dioxide Reduction Reaction

The electrochemical CO_2 reduction reaction (CO_2RR) can be used to produce high-energy density fuels and/or industrially relevant chemicals and is an attractive approach to reduce CO_2 emissions. Recently, Gu and co-workers showed cathodized MONs can acts as precursor materials for highly active CO_2RR catalysts.[101] The CO_2RR activity of $Cu_2(CuTCPP)$ MONs on a fluorine doped tin oxide electrode yielded formic and acetic acids with a cumulative Faradaic efficiency (FE) of $\approx 85.2\%$ and high TOFs of 2037 and 138 h^{-1}. This compared favorably with the electrode by itself which generated a negligible amount of CO with an FE of <10%. Detailed structural analysis revealed the $Cu_2(CuTCPP)$ MONs restructured to form CuO, Cu_2O, and Cu_4O_3 under catalytic conditions and these species were speculated to be real active catalysts. Even though the crystalline nature of the MONs was not preserved during restructuring, the TCPP ligand was believed to remain anchored to the copper oxide catalysts.

The Gu group also showed how post-synthetic functionalization of ZrBTB can be used to enhance CO_2RR.[102] Zr-BTB MONs were unable to catalyze CO_2RR to form CO by themselves. However, addition of bridging CoTCPP functional groups onto the surface of the ZrBTB MONs resulted in CO production with a faradaic efficiency of 77.2%. This was further enhanced through functionalization of the missing linkers defects in the Zr clusters with *p*-sulfamidobenzoic acid resulting in an increased CO Faradaic efficiency of 85%

and much lower Tafel slope values. In a related study, Lin and co-workers showed how post-synthetic functionalization of the Hf_6 clusters of Hf-TPY MONs with monodentate cobalt centered porphyrin functionalities could be used to enhance CO_2RR (Figure 4f).[103] The authors propose that co-operative interactions stabilize a highly active pyridinium-CO_2-Co species formed between the Co of the coordinated porphyrin unit and the protonated TPY ligand. The authors highlight that key to enhancing CO_2RR activity, is suppressing the competing HER. Zr-TPY/CoPP MONs showed enhanced CO/H_2 selectivity of 11.8 in comparison to the 2.7 for Zr-BTB/CoPP. Zr-TPY/CoPP also exhibited high CO-FE of 92.2% with a TOF of 0.40 s^{-1}.

2.4. Perspective

The most clearly demonstrated advantage of MONs over MOFs in catalysis are the enhanced yields and TON shown throughout the examples thanks to increased external surface area and exposed active sites of MONs compared to bulk MOFs. Comparisons with the equivalent homogeneous catalysts are less common, although the high density of active sites and ease of recovery from solution shows some promise here too. Stability is often touted as the barrier to the industrial application of MOFs as catalysts and it might be expected to be all the more problematic for MONs as atomically thin nanosheets. Some examples do show that MONs can degrade under catalytic conditions and the active species may not be those of the MON, highlighting the importance of fully characterizing the MONs following catalysis. However, other impressive examples such as those of the Hf and Zr MONs show that MONs can remain robust even under relatively harsh thermo-, photo- and electro-catalytic conditions.

The diverse chemistry of MONs has enabled them to catalyze a wide variety of reactions. MONs have been shown to catalyze reactions through coordinatively unsaturated metal ions at the center of porphyrins, the axial positions of paddlewheels and in Zr or Hf based clusters. The optical and electronic properties of linkers and metal ions also allow them to be used directly for photo- and electrocatalysis. However, although a diverse range of different MONs have been reported, most examples are clustered around a handful of core structures which have previously been reported to form nanosheets. This is probably partially a reflection of this being a relatively new area of research in which a small number of groups have made significant contributions and partly due to the difficulty of optimizing the synthesis of new MONs. We anticipate that with time examples of many other catalytically active MON architectures will come to prominence offering different activities.

In the majority of examples, known catalytic functional groups are attached to the surface of MONs post-synthetically. A wide range of organic functional groups and co-ordination complexes have been added to different MONs through post-metalation, ligand exchange or covalent attachment. Furthermore, the MONs can be combined with MNPs, enzymes, other nanosheets, polymers, and nanotubes. In some cases, these functionalities directly catalyze the reactions, but they can also enable chiral selectivity, act as light harvesting groups, enhance conductivity or electrochemical activity. Indeed, to our taste,

ADVANCED
SCIENCE NEWS
www.advancedsciencenews.com

ADVANCED
FUNCTIONAL
MATERIALS
www.afm-journal.de

the most exciting aspect of MON chemistry is this potential to bring multiple functional groups onto the surface of MONs in well-defined positions in order to create sophisticated active sites. Beautiful examples of the levels of complexity that can be achieved through multiple levels of post-synthetic functionalization have already been demonstrated.

3. Accessible Binding Sites for Sensing Applications

New sensors, with enhanced selectivity and sensitivity are needed to address global challenges such as monitoring atmospheric and environmental pollutants, the early diagnosis of diseases and detection of explosives. MONs possess a number of features which make them ideal for use in sensing applications. Their high external surface areas are easily accessible to analytes allowing for more rapid and sensitive detection. Unlike most other 2D materials, the easily modifiable structures of MONs mean each system can potentially be tailored to facilitate interactions between the target analytes and metal nodes, ligand functionalities, or species adsorbed onto MON surfaces. MONs can be employed as sensors in suspension, as thin films or within membranes, and can produce a variety of different optical and electronic responses. In this section we discuss current examples of MONs used in the sensing of small molecules, biological molecules, and metal ions. Examples of integrated electronic sensors are discussed in Section 4.

3.1. Small Molecules

Numerous authors have demonstrated the use of molecular interactions between analytes and the metal nodes of MONs to facilitate chemosensing. PW-based MONs have proven particularly effective in this regard as the PW unit possesses Lewis acidic axial sites, typically occupied by weakly coordinating solvent molecules that can be exchanged for Lewis basic analytes. A simple approach based on this was demonstrated by Qiu et al., who used a ZnBDC system to sense ethylamine via a ratiometric fluorescence-quenching mechanism, in which the organic amine binds to the PW via the N-donor.[5] Zhang et al. then used similar CuBDC nanosheets to selectively bind larger organic dye molecules with electron donor moieties, such as methyl orange, to open PW-sites (Figure 5a).[105] The authors also observed weaker binding in solvents with higher basicity, owing to the stronger MON-solvent interactions. However, the significant adsorption and selectivity was still observed, indicating the suitability of PW MONs for sensing such analytes.

In our own work, we demonstrated the sensing of small N-heterocycles with analogous CuBDC systems, functionalised with alkyl-ether chains at the 2- and 5- positions of the aromatic linker intended to aid exfoliation and dispersion.[7,106] UV–vis titrations were used to quantify the binding and MONs functionalised with pentyl chains were found to bind more strongly than those with methoxy-propyl chains, which was attributed to intramolecular binding of the oxygen lone pair. In a follow-up
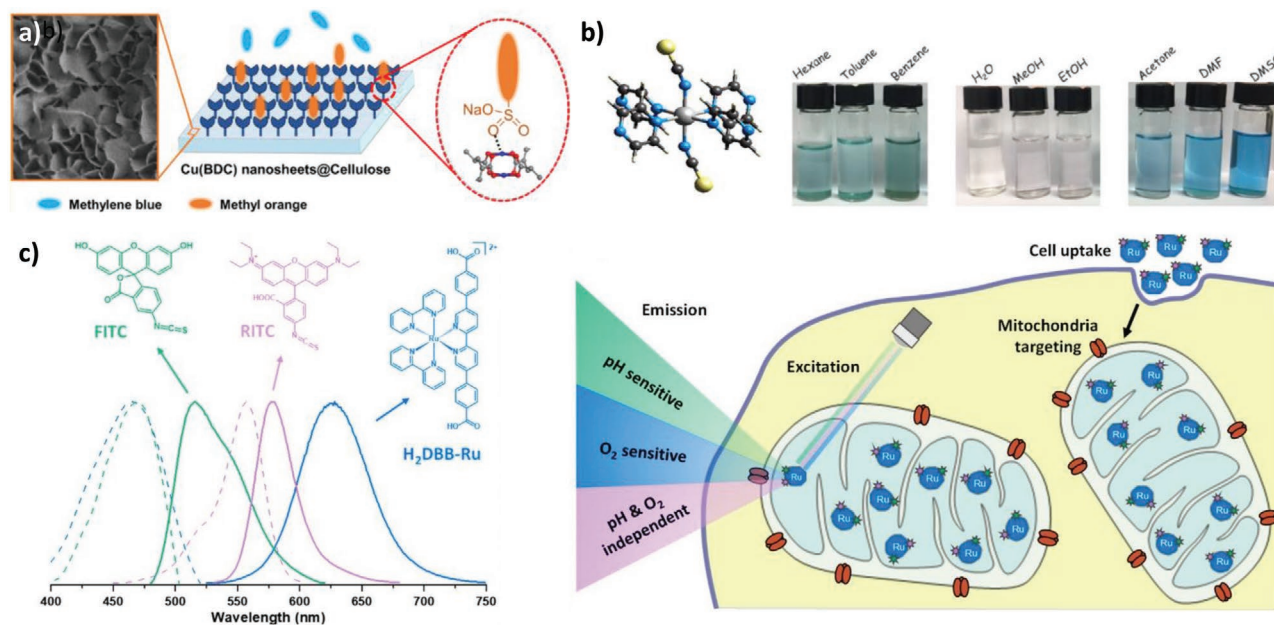
Figure 5. a) An illustration showing the preferred binding of methyl orange, via a pendant sulfonate group, over methylene blue to CuBDC nanosheets grown on cellulose by Zhang and co-workers. Reproduced with permission.[105] Copyright 2019, American Chemical Society. b) The chemical structure of the $Co(CNS)_2(pyz)_4$ unit used by Sun et al. to construct their MON system, and the color displays of colloidal suspensions of these MONs in selected nonpolar, protonic, and polar solvents. Reproduced with permission.[110] Copyright 2018, American Chemical Society. Further permissions related to this material excerpted should be directed to the ACS. c) Schematic showing the chemical structures and excitation/emission spectra of FITC, RITC, and H_2DBB-Ru. Used by Lin and co-workers, alongside an illustration demonstrating how positively charged Hf_{12}-Ru-F/R targets mitochondria and allows ratiometric sensing of intramitochondrial pH and oxygen via the luminescence ratios of pH-sensitive FITC to pH-independent RITC and O_2-sensitive DBB-Ru to O_2-independent RITC, respectively. Reproduced with permission.[112] Copyright 2019, American Chemical Society.

**ADVANCED
SCIENCE NEWS**

www.advancedsciencenews.com

**ADVANCED
FUNCTIONAL
MATERIALS**

www.afm-journal.de

study, we demonstrated that blending different linkers to create multivariate MONs could be used to fine tune their binding, as well as enhance their dispersion in different solvents.[107]

Other examples of small molecule sensing involve analytes interacting with linker functionalities rather than metal node sites. Several examples of fluorescent MONs which show enhancements or quenching of their fluorescence upon guest binding have been reported. Ma and co-workers created ultrathin MONs incorporating calix[4]arenes as fluorescent sensors for pesticides. The cavities of the calix[4]arene enabled host-guest interactions with glycophosphate leading to enhanced fluorescence with a detection limit of 0.38 ppm.[108] Cui and co-workers developed a MON system based on chiral 1,1′-binaphthol/-biphenol dicarboxylic acids, capable of enantioselective sensing.[55] The chiral −OH groups become exposed post-exfoliation, resulting in an enhanced fluorimetric sensing response for a series of chiral amino alcohols.

Moorthy and co-workers have demonstrated efficient sensing of nitroaromatics using a MON system based on a fluorescent 6-connecting hexa-acid linker.[109] Here, the fluorescence of the electron rich MON is quenched by increasingly electron deficient analytes, with trinitrotoluene the most deficient and most effective quencher. The coordination polymer only exhibits fluorescence when exfoliated, as the close-packed nature of the MOF causes self-quenching. The MON also demonstrates advantages over the free linker, both in quantum yield and quenching efficiency, which the authors attribute to the rigidification of the fluorophore linker, and to confinement of the analytes within the MON pores, indicating that the loss of three-dimensionality does not inhibit the use of host-guest pore chemistry.

Sun et al. developed a $Co(CNS)_2(pyz)_2$ (pyz = pyrazine) layered MOF, which when exfoliated, was capable of colorimetrically distinguishing between different classes of solvent (Figure 5b).[110] This was determined to be a result of the way that sulphur atoms on the coordinating thiocyanate groups exposed on the nanosheet surfaces interacted with solvents with different polarity and proton acidity. Tan and co-workers were able to use OX-1 nanosheets to distinguish between polar solvents with different sizes.[111] In this case the sensing mechanism was the disruption of host-guest interactions between the MON and a fluorescent zinc(II) bis(8-hydroxyquinoline) guest, leading to changes in emission. The MONs emission redshifted in the presence of nonpolar aliphatic solvents and halogenated solvents which was attributed to differences in their mobility and size respectively.

Perhaps one of the most intricate examples of small molecule sensing with MONs to date came from Lin et al. in 2019, who demonstrated simultaneous and ratiometric sensing of pH and O_2 in live cells using a coordinatively post-synthetically modified MON.[112] The DBB ligand was modified with a Ru photosensitizing complex pre-synthetically and two different dyes, fluorescein (FITC) and rhodamine B (RITC), modified with isothiocyanate groups were introduced to the Hf_{12} clusters via a post-synthetic modification of the Hf_{12} capping groups (Figure 5c). Both FITC and the Ru complex are pH and O_2 sensitive, respectively, whereas the RITC dye is independent of the concentration of both. Thus, by comparing the emission intensities of FITC and Ru to RITC, the concentration of pH and O_2 in live cells could be determined.

Several authors have used MONs as horseradish peroxidase mimics to facilitate sensing of H_2O_2, glucose, and other small molecules. In these reports, the role played by the MONs is as a catalyst for the reduction of H_2O_2, which in turn induces an electro- or photochemical response that is then detected. A simple but effective example of this was reported by Zheng et al., who used hybrid CuTCPP nanosheet and carbon nanotube (CNT) films to electrocatalytically reduce H_2O_2, producing an amperometric response with an impressive detection limit of 5 nM.[113] In this case the nanosheets directly catalyze the reduction, but other authors have used embedded MNPs and complexes as additives to enhance the catalysis.[114,115] The reduction of H_2O_2 can also be coupled with the oxidation of glucose by glucose oxidase (GOx) to detect the simple sugar, as demonstrated by Li and co-workers using luminescent In(AIP) MONs.[116] However, the more typical approach has been to couple the peroxidase activity of MONs with an oxidation-sensitive chromophore, including 3,3″,5,5″-tetramethylbenzidine (TMB),[117–119] o-phenylenediamine,[120] thiamine,[121] or luminol.[122] This sensor setup allows one to generate a colorimetric response upon detection of H_2O_2 or a corresponding analyte through redox chemistry. For example, Wang et al. used a system shown in **Figure 6**, constructed of PtNP/CuTCPP(Fe) hybrid nanosheets, GOx and TMB to develop a cascade colorimetric method capable of detecting H_2O_2 and glucose with excellent sensitivity and selectivity.[117] Although this same peroxidase mechanism can be achieved using other 2D materials, such as transition metal dichalcogenides,[123] MONs have demonstrated higher sensitivities and selectivities, shown in **Table 1**.

3.2. Biological Molecules

A well-established mechanism is the adsorption of fluorophore-labelled single-strand DNA (ssDNA) which is quenched by
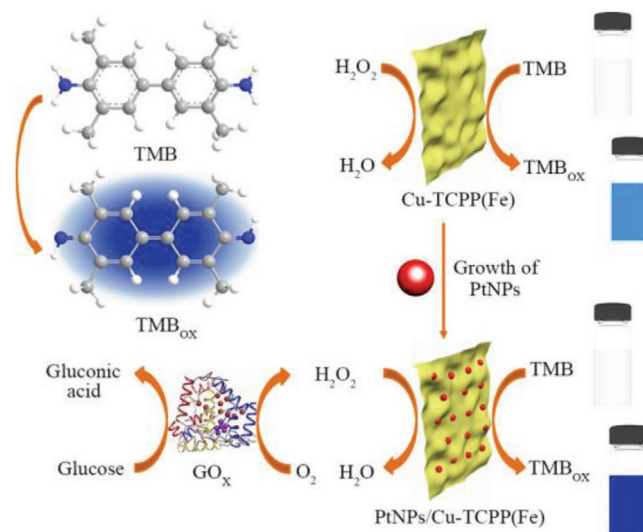

Figure 6. An illustration of the sensor developed by Ying and co-workers, using PtNPs/Cu-TCPP(Fe) hybrid nanosheets, GOx, and TMB and the mechanism by which it achieves colorimetric detection of both H_2O_2 and glucose. Reproduced with permission.[117] Copyright 2018, American Chemical Society.

**ADVANCED
SCIENCE NEWS**
www.advancedsciencenews.com

**ADVANCED
FUNCTIONAL
MATERIALS**
www.afm-journal.de

Table 1. Horseradish peroxidase activities of reported MONs, alongside other selected high performing nanoparticles and MOFs.

MON system	Response type	Additives	Analyte(s)	Limit of detection/μM	Linear range/μM	Ref.
CuTCPP	Amperometric	CNTs	H_2O_2	0.005	0.01–3.75	[113]
CuTCPP	Amperometric	CNTs	H_2O_2	0.7	0.001–8.159	[124]
CuTCPP	Amperometric	Ag NPs	H_2O_2	1.2	0.0037–5.8	[114]
CuTCPP(Fe)	Colorimetric	Pt NPs, TMB, GOx	H_2O_2	0.357	2–100	[117]
			Glucose	0.994	2–200	
CoTCPP(Fe)	Chemiluminescence	Luminol, GOx	Glucose	0.06	0.18–30	[127]
NiBDC	Colorimetric	TMB	H_2O_2	0.008	0.04–160	[118]
NiBDC	Amperometric	Hemin	H_2O_2	0.2	1–400	[115]
InAIP	Fluorimetric	–	H_2O_2	0.87	0–160	[116]
Cu(HBTC)	Colorimetric	Fe_3O_4-AuNPs, TMB, ssDNA	H_2O_2	0.0011	0.00286–0.07143	[124]
			Glucose	12.2	12.86–257.14	
			Sulfadimethoxine	0.005	0.01–1.15	
CuABDC	Fluorimetric	TMB, xanthine oxidase, OPD	Hypoxanthine	3.93	10–2000	[120]
$Cu(BPY)_2(OTf)_2$	Fluorimetric	Thiamin, GOx	Glucose	0.41	10–100 and 100–1000	[121]
Other Systems						
Titania NPs	Colorimetric	–	H_2O_2	0.5	1–1000	[125]
MIL-68 / MIL-100	Colorimetric	TMB	H_2O_2	0.256/0.155	3.0–40	[126]

MON systems, initiating a signal-on response in the presence of its complimentary strand. Zhao and co-workers have shown that simple organic dyes, such as Rhodamine B, bind to MONs because of spontaneous and hydrophobic forces followed by a quenching of their emission, meaning this approach is broadly applicable to any ssDNA with a fluorescent tag.[127] This has been demonstrated numerous times as a simple and selective mechanism for the targeted detection of DNA, as shown in **Figure 7**a. Zhang et al. were the first to document this, exploiting the accessible and anisotropic structure of a CuTCPP system to efficiently quench the emission of Texas red-labelled ssDNA.[128] Several tests demonstrated that this fluorescence quenching was a direct result of the 2D nature of the MONs and their surface interactions, as both the H_6TCPP ligand and the bulk layered MOF had significantly reduced quenching efficiencies. The MON-based DNA bioassay was then used for the simultaneous detection of the Influenza A virus sub-type H5N1 gene and subtype H1N1 gene by using Texas Red-labelled ssDNA and tetrafluororescein-labelled ssDNA probes. The introduction of the target DNA selectively recovered the fluorescence of the respective probe.

Since these early studies, multiple authors have reported related studies which make use of MONs as a platform to quench the fluorescence of ssDNA based probes.[129–131] In particular, Lei and Zheng et al. identified coordination from electron donor groups on the DNA-fluorophores to open Fe^{2+} sites present in their Hofmann-type nanosheets leading to ligand to metal charge transfer which quenched the fluorescence (Figure 7b). The analogous 3D MOF showed a reduced quenching efficiency compared to the nanosheets as the majority of surface accessible metal sites are unaccessible.[132] Interactions between surface-accessible metal sites and the DNA-fluorophores have been highlighted by other authors as potentially key to explaining the increased quenching efficiency

of MONs compared to other 2D materials and 3D MOFs.[133] Xia and co-workers reported a two-color sensing platform for DNA by using two dye labels which interacted differently with their lanthanide-based (Ln) MONs.[134] The fluorescence of ssDNA labelled with fluorescein amidite (FAM), carrying negative charges, was only partially quenched by Ln-MONs. When hybridized with the complementary target DNA, the FAM-dsDNA detached from the surface of the nanosheets and reattached to the edge of the nanosheets via an electrostatic interaction between FAM and Ln^{3+}. In contrast, the ssDNA labelled with 5-carboxytetramethylrhodamine, carrying positive charges, showed the same quenching and recovery properties on MOF-Ln nanosheets as observed with traditional 2D materials. It was also observed that lanthanum-based MONs exhibited superior fluorescence quenching abilities to the neodymium, europium, and terbium-based MONs due to the lanthanide contraction.

Electrochemiluminescence (ECL) is often cited as a more sensitive response-type than fluorescence in the broader sensing literature, and multiple authors have exploited the redox chemistry of MONs to demonstrate this.[135] In particular, Dong-Rong Xiao and co-workers have used MONs based on aggregation induced emission (AIE) ligands to develop ECL platforms that are quenched by ferrocene-tagged ssDNA.[136,137] These systems are another example of how enhanced functionality can be built into MON systems through rational design. The AIE ligand MONs exhibit increased sensitivity and ECL intensity compared to the layered MOFs, ligand aggregates and ligand monomers. These systems are some of many reports in which current biosensing technologies are employed to increase the biosensors sensitivity. For example, to facilitate detection of the carcinoembryonic antigen down to 0.63 fg mL^{-1}, Xiao et al. use a rolling circle replication in order to produce duplicate DNA fragments which, form the complimentary ssDNA.
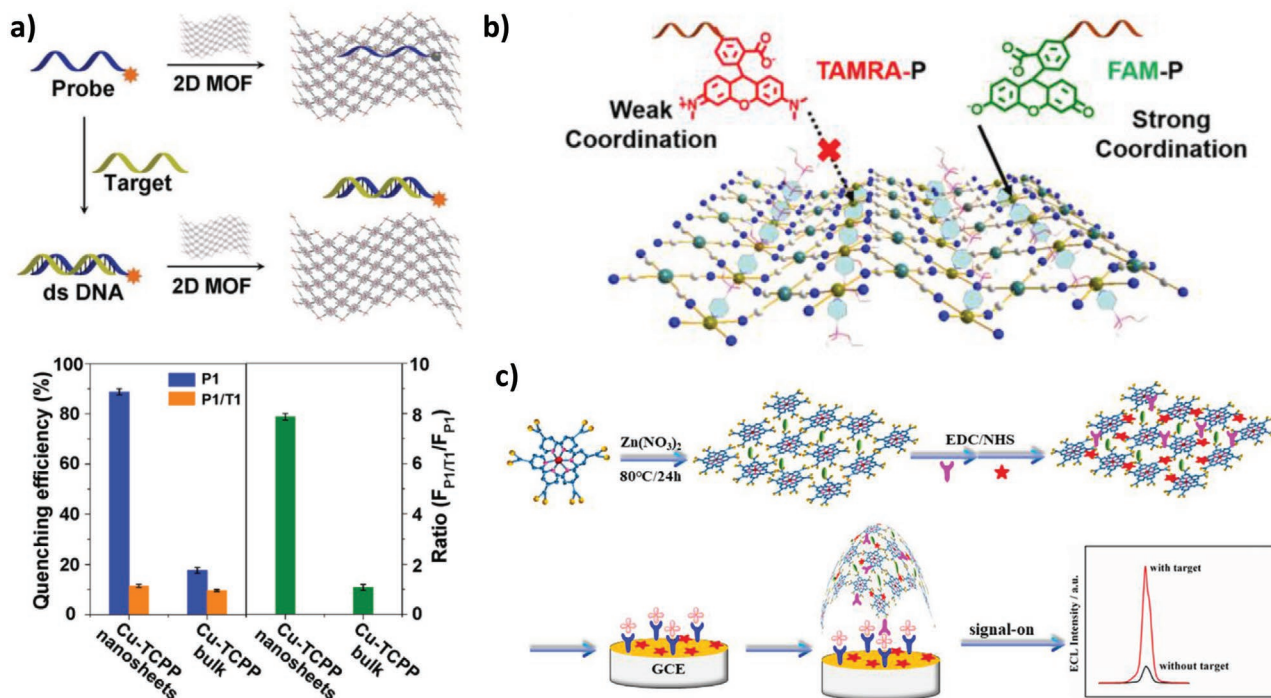
Figure 7. a) An illustration of a MON-based fluorescent DNA assay and bar chart showing Left: The quenching efficiency of CuTCPP nanosheets and bulk CuTCPP MOFs for P1 and P1/T1. Right: The fluorescence intensity ratio at 609 nm in the presence of CuTCPP nanosheets or bulk CuTCPP MOFs. $F_{P1/T1}$ is the fluorescence intensity of dsDNA (P1/T1) at 609 nm and F_{P1} is the fluorescence intensity of ssDNA (P1) at 609 nm. Reproduced with permission.[128] Copyright 2015, Wiley. b) A schematic illustration showing the differing interactions of nanosheets developed by Lei and co-workers with TAMRA-labelled and FAM-labelled ssDNA. Reproduced with permission.[132] Copyright 2019, American Chemical Society. c) An illustration depicting the construction and mechanism of the signal-on ECL immunosensor developed by Huang and Yang et al. for the detection of Cardiac Troponin I. Reproduced with permission.[138] Copyright 2019, American Chemical Society.

Although the immobilization of labelled-DNA strands is one of the most common bio-sensing mechanisms in the 2D materials literature, the use of antibody and enzyme-based biosensors can be significantly more selective and effective in the monitoring of some diseases. Yang and Huang et al. have demonstrated antibody-immobilization onto MONs, utilizing a Ru(DCBPY) system to construct a signal-on ECL immunosensor (Figure 7c).[138] In this case, the use of MONs allows the facile incorporation of redox-active species (in this case Ru), meaning signal-outputs such as ECL can be easily incorporated into the final sensor, a factor that has also been utilized by Xiao et al. in the detection of mucin 1 using a DNA assay.[139] A separate report by Xia et al. utilizes the high aspect ratios of CuTCPP(Fe) MONs to immobilize both PtNi nanoparticles and antibodies onto their surfaces, thus constructing a sandwich-type electrochemical immunosensor for calprotectin in serum. In this study, the nanoparticle/MON hybrid structure exhibits enhanced electrocatalytic activity towards H_2O_2 reduction, enabling them to act as signal amplifiers resulting in the highly sensitive detection of calprotectin down to 137.7 fg mL^{-1}.[140]

3.3. Ions

To date, the sensing of solution-phase ions with MONs is limited to a handful of examples, the majority of which have only explored the sensing of Fe^{3+} ions. The first example of

Fe^{3+} sensing with MONs was demonstrated by Qian et al. in 2016, who showed that $Ti_2(HDOBDC)_2(H_2DOBDC)$ nanosheets exhibited a fluorescence quenching response in the presence of Fe^{3+} ions.[141] This was attributed to competitive absorption in the UV–vis region, and potential electron transfer between Fe^{3+} and the MONs. The authors also demonstrated that the highly dispersive nature of the nanosheets allows close contact between them and the metal ions, leading to reduced limits of detection compared to bulky MOF sensors and other nanomaterials. The same fluorescence quenching mechanism of Fe^{3+} sensing has since been demonstrated with other nanosheets systems, also exhibiting improved detection limits.[142,143] However, although each of these systems has been demonstrated to be selective amongst a range of transition metal ions, this mechanism of detection is potentially hindered by the presence of other species present that absorb in the same region of the UV–vis spectrum. This is partially demonstrated by Ni and Sang et al., who observed that their $Zn_2(bim)_4$ system was capable of sensing Fe^{3+} via this mechanism, but Cr^{3+} also exhibited a similar but reduced quenching effect. Furthermore, Chen and co-workers observed that Zn(5-(4-pyridyl)-tetrazolyl) MONs can sense but cannot distinguish between both Fe^{3+} and Cu^{2+} ions.[144]

In 2019, Hmadeh et al. demonstrated a comparable turn-off probe for Pd^{2+} with isonicotinate-based AUBM-6 nanosheets.[107] In this case, it was shown that the unexfoliated layered MOF exhibits a significantly reduced fluorescence intensity, and thus
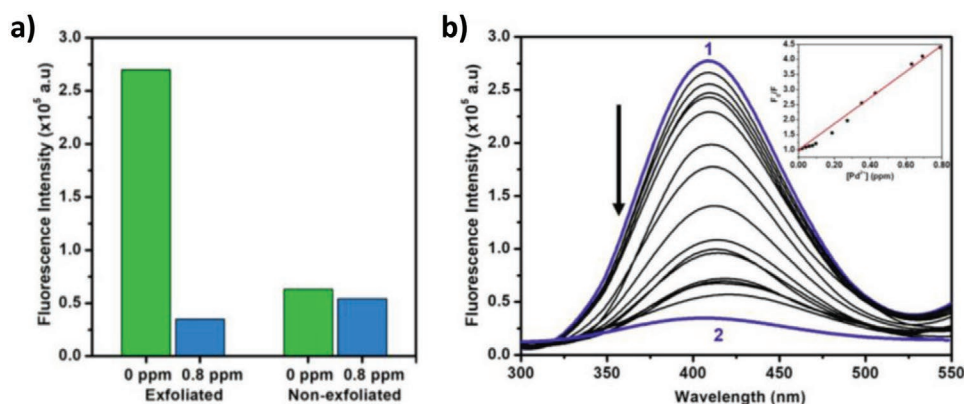
**ADVANCED
SCIENCE NEWS**

www.advancedsciencenews.com

**ADVANCED
FUNCTIONAL
MATERIALS**

www.afm-journal.de

Figure 8. a) The effect of exfoliation of AUBM-6 MOF into nanosheets on the sensing of Pd^{2+} at 0.8 ppm. b) Photoluminescence spectra of AUBM-6 MONs. PL titrations of AUBM-6 at 1) 0 and 2) 0.8 ppm of Pd^{2+} ions at $\lambda_{ex} = 285$ nm. (inset) Stern–Volmer plot demonstrating gradual Pd^{2+} titrations. Reproduced with permission.[107] Copyright 2019, American Chemical Society.

is much less sensitive to changes in the concentration of Pd^{2+}, as shown in **Figure 8**. However, the fluorescence of this system is also sensitive to the presence of As^{3+}, Cu^{2+}, and Fe^{3+} ions, albeit to a lesser degree.

3.4. Perspective

The current literature on the use of MONs in the development of novel sensors broadly divides into one of two approaches. The first approach involves the design of MONs as the complete active sensor with analytes interacting directly with the MONs surface and so inducing observable changes in the MONs optical or electronic properties. The diverse chemistry of MONs mean that they can play many different roles within these interactions with open metal sites binding analytes, catalyzing reactions or acting as redox sites and ligands acting as hosts to quench or enhance fluorescence. The porosity of MONs can also be exploited by creating cavities to enhance guest binding. The outputs can be diverse with changes in color, fluorescence or an electrochemical response. The second approach uses MONs as just one component within often complex, well established, multicomponent sensor systems. In these examples, much of the sensitivity and selectivity often comes from other components within the system such as single-stranded DNA, enzymes or nanoparticles.

Multiple reports have demonstrated the enhanced sensitivity and response times of MONs compared to MOFs thanks to their increased accessibility of their binding sites. Although the higher surface area of MONs is advantageous in sensing, this must also be coupled with a highly sensitive method of detection such as fluorescence, ECL or electrochemistry to

create a competitive sensor. Another advantage is the potential for improved response times compared to bulk MOFs where access to binding sites can be diffusion limited, however this has not yet fully been demonstrated. The density of active metal and ligand binding sites on MONs is also a potential advantage compared to solution-based sensors, particularly for larger analytes where multiple interactions can occur. The selectivity introduced by the MONs in most of the examples above is limited to generic binding interactions such as co-ordination to metal sites or quenching of fluorophores. In our opinion, only a few examples so far demonstrate the full potential of MONs as a platform for creating specific binding sites within effective sensors.

4. Tunable Opto-Electronic Properties for Energy Storage, Light Harvesting, and Other Devices

The silicon-centered paradigm in electronics has recently been challenged by the commercialization of organic light emitting device (OLED) technology, rapid developments in hybrid perovskites for solar cells and new types of graphene based integrated photonics. The diverse chemistry and modular structure of MONs allows for ready tuning of a diverse range of useful electronic and optical properties including their dielectric constants,[145] electrical resistance,[146] redox activity and band gap.[40,147–149] Although most MONs are insulating, there are a growing number of 2D architectures which show semi-conducting and conducting behavior. The nanoscopic dimensions of MONs allow for integration within thin-film devices in a way not possible for bulk MOFs.[150] This section focuses on the progress that has been made in the use

Table 2. MON based metal-ion batteries and their performance parameters.

MON	Diffusion coefficient [cm^2 s^{-1}]	Rate capability [mAh g^{-1} at 2 A g^{-1}]	Reversible capacity [mAh g^{-1}]	Cycles tested	Ref.
Mn-UMOFNs	2.48×10^{-9}	701	1187	100	[159]
Ni-UMOFNs	3.77×10^{-9}	229	546	100	[159]
u-CoTDA MONs	Not reported	694	790	400	[158]
Zn-LMOFNs	Not reported	525	623	100	[160]

Table 3. MON based supercapacitors and their performance parameters.

MON	Specific capacitance [F g^{-1}]	Current density (A g^{-1})	Cycling capacity [%]	Cycles tested	Energy density	Power density	Ref.
NiCoMOF/rGO	1553	1	83.60	5000	44 Wh kg^{-1}	3168 W kg^{-1}	[167]
CuTCPP/PPy	163.34	0.2	n/a	n/a	2.27 µWh cm^{-2}	50 µW cm^{-2}	[168]
NiTCPP/CNT	2280	5	90.3	2000	n/a	n/a	[113]
NiCo-BDC	2230	1	68.5	6000	34.3 Wh kg^{-1}	375 W kg^{-1}	[164]
Co$_2$(OH)$_2$C$_8$H$_4$O$_4$	2564	1	95.8	3000	n/a	n/a	[163]
NiCo-MOF@PNTs	1109	0.5	79.10	10 000	41.2 Wh kg^{-1}	375 W kg^{-1}	[169]
Ni-Co BDC	1700.40	1	93.2	2000	n/a	n/a	[165]
CuBTC@MnO$_2$	340	1	95	6000	n/a	n/a	[170]
NiCo-PTA MON	1202.1	1	n/a	n/a	49.4	562.5	[166]

of MONs within electronic sensors, batteries, supercapacitors, light emitting diodes, and photovoltaics.

4.1. Device-Integrated Sensors

MONs have been cast as films onto interdigitated electrodes and used as chemresistive sensors to monitor analytes based on changes in their electrical resistance. Dinca and co-workers demonstrated the use of conductive MONs of Cu$_3$(HITP)$_2$ (HITP = hexaminotriphenylene) as ammonia sensors via potentiostatic measurements (**Figure 9**a).[154] These MONs with intrinsic pi-conjugation and charge de-localization within the plane, showed a conductivity of 0.2 S cm^{-1}. Similar chemresistive sensors developed using isomorphic Ni$_3$(HITP)$_2$ and Cu$_3$(HHTP)$_2$ MONs (HHTP = 2,3,6,7,10,11-hexahydroxytriphenylene) were shown to reliably distinguish between different categories of volatile organic compounds. The authors attributed either charge transfer or hydrogen bonding as

the possible mechanisms for the various sensing responses observed.[151]

Zhao and co-workers used first principles calculation to show that the selectivity of semiconducting MONs towards gas sensing arose from the increased electronic states near the fermi level due to adsorption of the gas molecules onto MONs (Figure 9c). The authors stated that the resulting up-shifted fermi level is expected to change the electronic property of the MONs from semi-conducting to metallic—leading to the chemresistive response.[152]

Non-conductive MONs have also been used in combination with conductive substrates to make electronic sensors. Hu and co-workers demonstrated the use of NiBDC MONs when composited with Ni/NiO/C as a non-enzymatic glucose sensor with high sensitivity of 367.45 mA M^{-1} cm^{-2} (Figure 9b).[153] Other notable examples include CoTCPP(Fe) MONs as amperometric sensors for H$_2$O$_2$ detection, AuNCs@521-MOF (where NC = nanocrystal) for detection of cocaine by electrochemical impedance spectroscopy and ZnTCPP MONs for amperometric sensing of nitrite.[154–156]
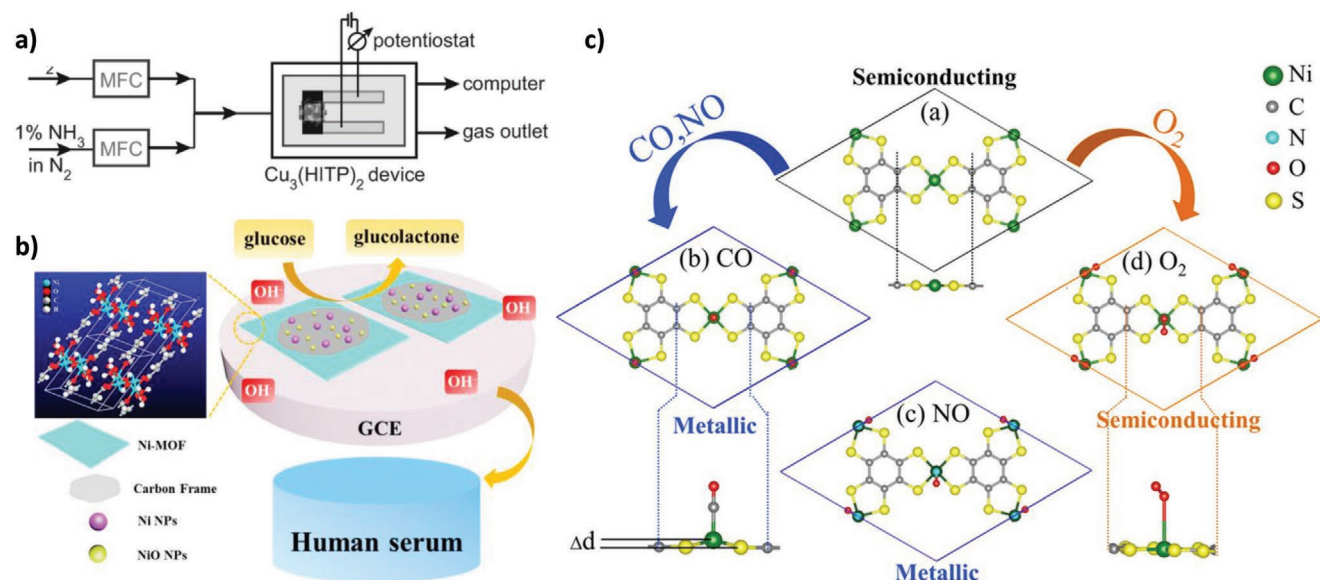
Figure 9. a) Scheme of a MON based chem-resistive device for ammonia sensing. Reproduced with permission.[154] Copyright 2015, Wiley. b) Schematic of the Ni-MOF/Ni/NiO/C nanocomposite glucose sensor for human serum samples. Reproduced with permission.[153] Copyright 2017, America Chemical Society. c) Schematic representation of change in electronic nature of MONs upon gas adsorption. Reproduced with permission.[153] Copyright 2016, American Chemical Society.
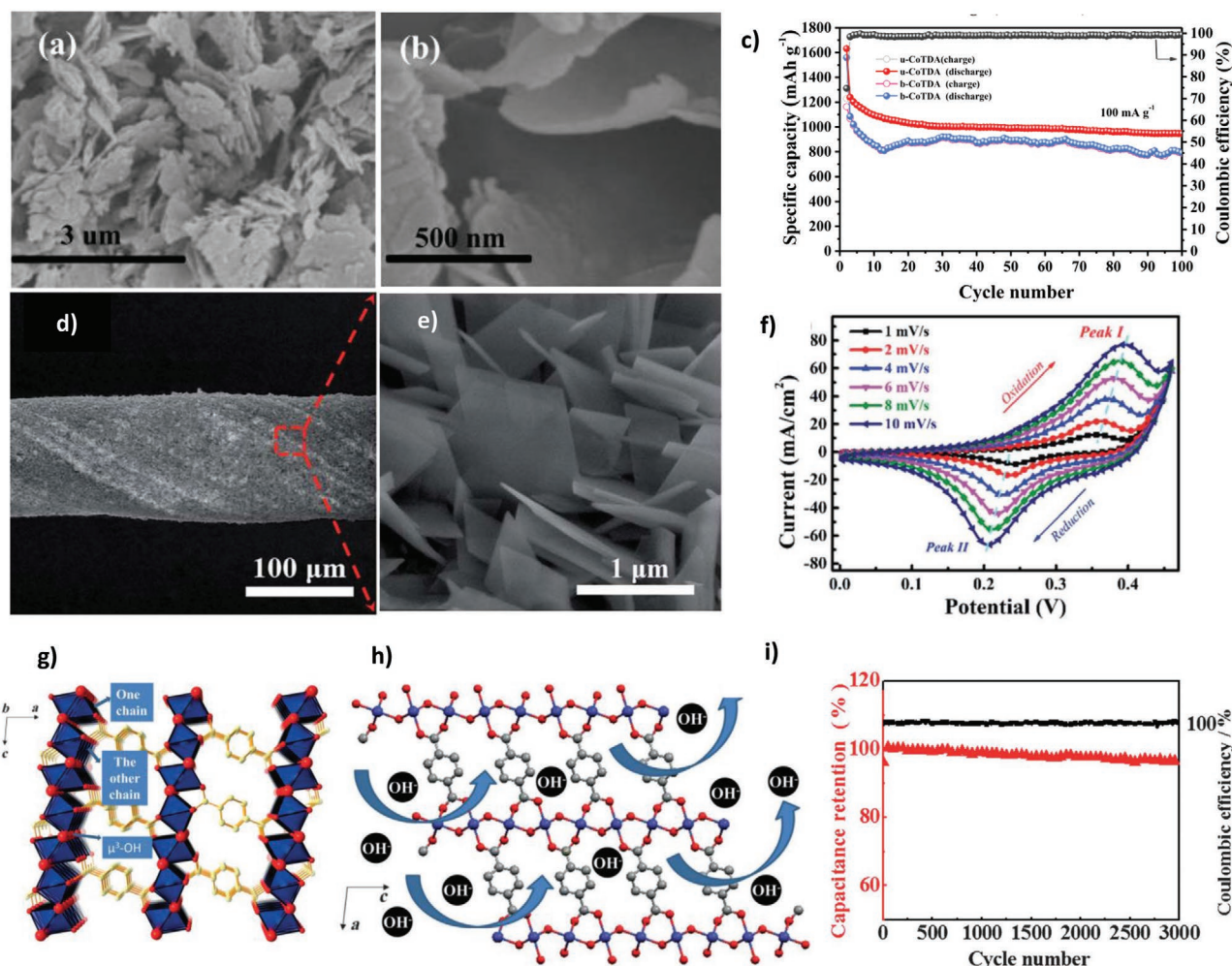
**ADVANCED
SCIENCE NEWS**

www.advancedsciencenews.com

**ADVANCED
FUNCTIONAL
MATERIALS**

www.afm-journal.de

Figure 10. a,b) SEM images of Co-TDA MONs employed as anodes in lithium ion batteries. c) Cycling performance of CoTDA MONs (u-CoTDA) compared with the bulk MOF (b-CoTDA) at a current density of 100 mA g^{-1} versus Li+/Li with the corresponding coulombic efficiency. a–c) Reproduced with permission.[158] Copyright 2017, Wiley. d,e) SEM images of Ni-MOF/CNTF showing nanostructured hybrid composites of MONs. f) The cyclic voltammetry curve of the corresponding MON based FAR Ni-Zn battery. d–f) Reproduced with permission of the Royal Society of Chemistry.[161] g) Structure of the Co MON with a layered structure and a conductive network frame used as a supercapacitor electrode. h) Schematic representation of intercalation/de-intercalation process of OH^{-1} in the layered structure of the Co-MOF crystal. i) Charge–discharge profile (black line) and specific capacitance (red line) at a current density of 2 A g^{-1} of the Co-MOF electrode. Reproduced with permission.[163] Copyright 2016, Wiley.

Layered MOFs have also been assembled as a transducer device for molecular recognition via capacitive response. NH$_2$-MIL-53(Al) was synthesized as nanosheets and nanoparticles by Gascon et al. using surfactant-assisted arrested crystallization technique. The nanosheets were cast as films over p-doped silicon substrates to obtain planar capacitive electrodes.[157] The authors showed that anisotropic structure of the nanosheets orientated the 1D channels with respect to the electrodes resulting in shorter diffusion pathways and so better capacitive sensing with reduced response time.

4.2. Electrodes for Energy Storage

MONs have been explored as potential electrode materials in lithium-ion batteries (LIB). The accessible redox active centres in MONs offer enhanced Li$^+$ ion insertion/desertion when used

within the anodes of LIB. Hu and co-workers demonstrated this strategy with (Ni$_2$(OH)$_2$BDC) MONs, (Mn$_2$(OH)$_2$BDC) MONs, and cobalt thiophenedicarboxylic acid MONs (**Figure 10**a–c).[158,159] The authors proposed that the lithiation/de-lithiation mechanism in these systems showed the involvement of both the metal center and the chelating ligands in the reduction/oxidation process, thereby providing a high theoretical electron storage capacity for the electrode. The ultra-thin morphology of the MONs offered shorter ion diffusion distances to the internal electroactive sites. This effective ion transportation in the MON based anodes resulted in 100% coulombic efficiency, outstanding rate capability, and long-term cyclic performance—key performance parameters in LIBs.[158–160]

MONs have also been used in conjunction with conductive supports to form high performing hybrid electrodes. Yao et al. demonstrated the use of nickel 2,6-naphthalene dicarboxylic acid (Ni-2,6 NDC) MONs grown on CNT fibers as a barrier

**ADVANCED
SCIENCE NEWS**

www.advancedsciencenews.com

**ADVANCED
FUNCTIONAL
MATERIALS**

www.afm-journal.de

free cathode to form a fiber-aqueous rechargeable nickel-zinc (FAR Ni-Zn) battery (Figure 10d–f).[161] The prepared device displayed high rate capacity and stability with up to 89% retention in capacity after 600 cycles of operation. Zong and co-workers studied the use of bimetallic porphyrin MONs/reduced graphene oxide (CoNi-MON/rGO) composite as the air electrode in zinc-air batteries. The authors attributed the superior performance and stability of this electrode to the optimized electronic conductivity of the bifunctional MON/rGO composite.[162]

MONs with high electrical conductivity have been reported as high performing electrodes in supercapacitors. Wei et al. demonstrated the pseudocapacitive behavior of conductive Co-MOF nanosheets (Figure 10g–i).[163] The study showed that the large interlayer distance in the MON structure provided enough space for electrolyte storage and ensured efficient OH^- intercalation and de-intercalation. The conductive network frame acted as an electron transport channel. The authors demonstrated that with a conductivity of 3.75×10^{-3} S cm^{-1}, the MONs helped accelerate the transfer of electrons at the electrode-electrolyte interface. Bu and co-workers demonstrated faradaic properties in a Ni-Co bimetallic MOF electrode deposited on Ni foam. This electrode showed lower series resistance and faster electron transfer rate during the charge/discharge procedure.[164] The electrochemical performance was shown to be better than the single ion MOFs due to the improved conductivity. In another study by Li and group, Ni-Co BDC MONs displayed strong coupling between the Ni^{2+} and Co^{2+} species which facilitated charge transfer during electrochemical reaction leading to high pseudocapacitive behavior.[165] Ni-Co BDC MONs on activated carbon were used to create asymmetric supercapacitors in another similar work by Yang et al.[166]

With a vast number of MONs exhibiting limited electrical conductivity, compositing them with other conductive nanomaterials is also a typical approach in supercapacitors. Zheng and co-workers demonstrated that NiTCPP film/CNT composites exhibit 1.8 times and 14 times higher specific capacitance than pure NiTCPP and pure CNT electrodes respectively.[113] The authors showed that the hybrid nanostructures reduced the aggregation of individual components and provided a shorter route between each component thereby improving electron transfer. Liu and co-workers developed 2D NiCo-MOF ultrathin nanosheets/rGO hybrid electrode. The authors showed that the rGO facilitated the ionic and electronic conductive pathway while the redox active sites of the MONs provided an additional pseudocapacitive component.[167] Zhang et al. demonstrated electrostatically self-assembled TCPP/GO electrode as a flexible asymmetric supercapacitor. The electropositive TCPP MONs and electronegative GO sheets when composited together showed bending tolerance and good conductivity.[171]

MONs have also been employed as substrates to host electrode materials. Zhao et al. demonstrated the electrochemical polymerization of polypyrrole (PPy) onto wrinkled 2D ultrathin CuTCPP nanosheets to construct a flexible CuTCPP/PPy hybrid film. The authors attributed the enhanced supercapacitive performance to intense electronic interaction between the CuTCPP MONs and PPy and the porous film structure that facilitated sufficient immersion of the electrolyte.[168] Detailed mechanistic investigations showed that PPy offered a conductive network for fast electron transport and enhanced the electrochemical kinetics. In a similar work, PPy nanotubes have also shown

success when used in conjunction with MONs to impede aggregation, boost conductivity and enhance the pseudocapacitance behavior.[169] In another example, Pang and co-workers used the porous Cu-BTC MON as an inert host for pseudocapacitive MnO_2 NPs. The authors attributed the resulting superior charge–discharge performance to the film formation in the MON/NPs composite that favored the diffusion path of ions.[170]

4.3. Memory Devices

Resistive random-access memory (R-RAM) devices are nonvolatile memory devices with a resistive-switching material as the active layer. Ding et al. showed how ZnTCPP MONs could be used to fabricate R-RAM devices which show bipolar resistive switching behaviour. In this work by ZnTCPP MONs are immobilized as guest in PVP polymer and cast as the resistive layer between two electrodes (**Figure 11**).[145] Differences in molecular orbital levels mean the MONs trap charge carriers within the insulating matrix. Once a high enough concentration of carriers is reached, charges can hop via the percolation pathways created by the MONs switching the device to a low-resistive state. Applying an electric field with reverse polarity leads to the collapse of the transport pathways and switches the device back to a high resistive state.

4.4. Metal-Organic Framework Nanosheets in Light Emitting Devices

In recent years, MONs have been used to create light emitting devices. In a work by Nishihara and co-workers, bis(dithiolato) nickel (NiDT) nanosheets on ITO were employed as the hole buffer layer within OLEDs. The devices showed comparable efficiencies to conventional OLEDs and nearly twofold enhancement in device lifetime compared to the standard PEDOT:PSS based devices.[172] Another promising example of MONs in emissive applications is by Lin et al. who used Zr-4′,4″,4‴,4⁗-(ethene-1,1,2,2-tetrayl)tetrakis([1,1′-biphenyl]-4-carboxylate-(TCBPE) based MONs to create visible light communication devices.[173] The bi-layered nanosheets display favorable photophysical properties, high quantum yields and restricted internal motion of the fluorescent struts owing to the network structure. However, there is a drop of 30% in output power following 168 h of operation, which the authors attribute to degradation of the linker upon light-exposure in the presence of oxygen.

4.5. Metal-Organic Framework Nanosheets in Photovoltaic Devices

The first example of MONs used in a functional solar cell was as a buffer layer in a paper by Huang and co-workers in 2018. Tellurophene based MON was mixed with a polymer surfactant PEIE (polyethylenimine ethoxylate) to form a hybrid ink that was integrated as an electron extraction layer along with ZnO into organic solar cells (**Figure 12**a).[174] Ultraviolet photoelectron spectroscopy measurements showed that the work function of ZnO decreased with the addition of PEIE,

ADVANCED
SCIENCE NEWS
www.advancedsciencenews.com

ADVANCED
FUNCTIONAL
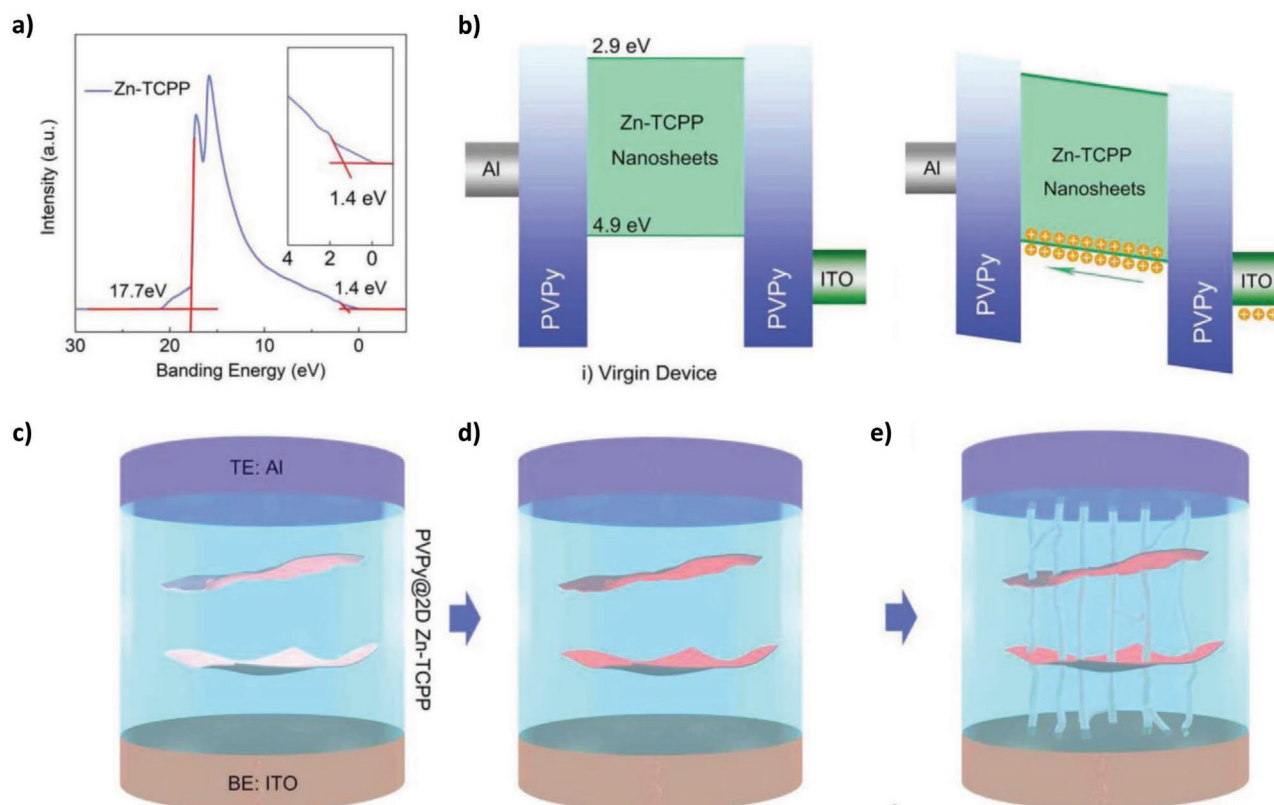**MATERIALS**
www.afm-journal.de

Figure 11. a) UPS measurement of ZnTCPP MONs used as memory device; b) the corresponding energy band diagram; and c–e) an illustration of resistance switching mechanism based on charge trapping. Reproduced with permission.[145] Copyright 2018, Wiley.

whilst adding the MONs increased it to a medium work function that improved device performance. The study showed this as a widely applicable approach by employing this MON based electron extraction layer in two important types of solar cells—P3HT-PCBM the workhorse of semiconducting devices—the most well characterized and largely accepted standard organic photovoltaics (OPV);[175] and PBDB-T-ITIC the best performing non-fullerene OPV at the time.[176] MONs have also been used to form a liquid-junction solar cell. Jiang et al. showed that porphyrin-based MONs could be assembled onto ITO and embedded with fullerenes to form a functioning device. The high surface area and porous structure of the photoactive MONs enhanced charge transfer to the electron accepting fullerenes resulting in a quantum efficiency of <0.5% (Figure 12b).[177]

A study published by our group is the first example showing incorporation of MONs into the photoactive layer of OPV bulk heterojunctions (Figure 12c,d).[178] Porphyrin MONs as a ternary blend within the archetypal P3HT-PCBM architecture resulted in the formation of a ternary blend solar cell which showed a doubling in device power conversion efficiency (PCE).[178] Detailed investigations into the morphology of the active layer using AFM, wide angle X-ray, and dark injection measurements showed that the relative proportion of crystalline regions in the thin films is improved upon incorporation of MONs. Thus, MONs act as templates to increase the crystallinity of the otherwise semi-crystalline polymer P3HT leading to more balanced charge mobility and device performance metrics.

Recently, Jen and co-workers demonstrated the use of MONs as an electron extraction layer at the perovskite/cathode interface leading to a 22.02% efficient perovskite solar cell (Figure 12e–g).[179] The MONs enabled improved long-term operational stability with up to 90% retention in PCE under accelerated testing conditions. The thiol functionalized Zr-BTB MON formed intimate contact with the silver electrode to extract electrons efficiently from the perovskite solar cell. The authors also demonstrated that the thiol functionalization trapped the mobile Pb^{2+} ions at the perovskite/electrode interface—a major step to mitigate the potential impact of perovskites on environmental sustainability.

4.6. Perspective

The growing number of examples of 2D conducting and semi-conducting MOFs offer significant opportunities for use within device-integrated sensors. The high surface area, inherent porosity, and ease of thin film formation of MONs offers advantages over other 2D materials and 3D frameworks. However, only a handful of conductive SBUs are so far known and the requirement to maintain extended conjugation limits the scope for enhancing the selectivity of these devices. The ultrathin nature of MONs allow for close contact between MONs and conductive supports opening up the use of a diverse array of insulating MONs within device integrated sensors.

MONs have already been shown to outperform their bulk counterparts when incorporated as electrodes in energy storage
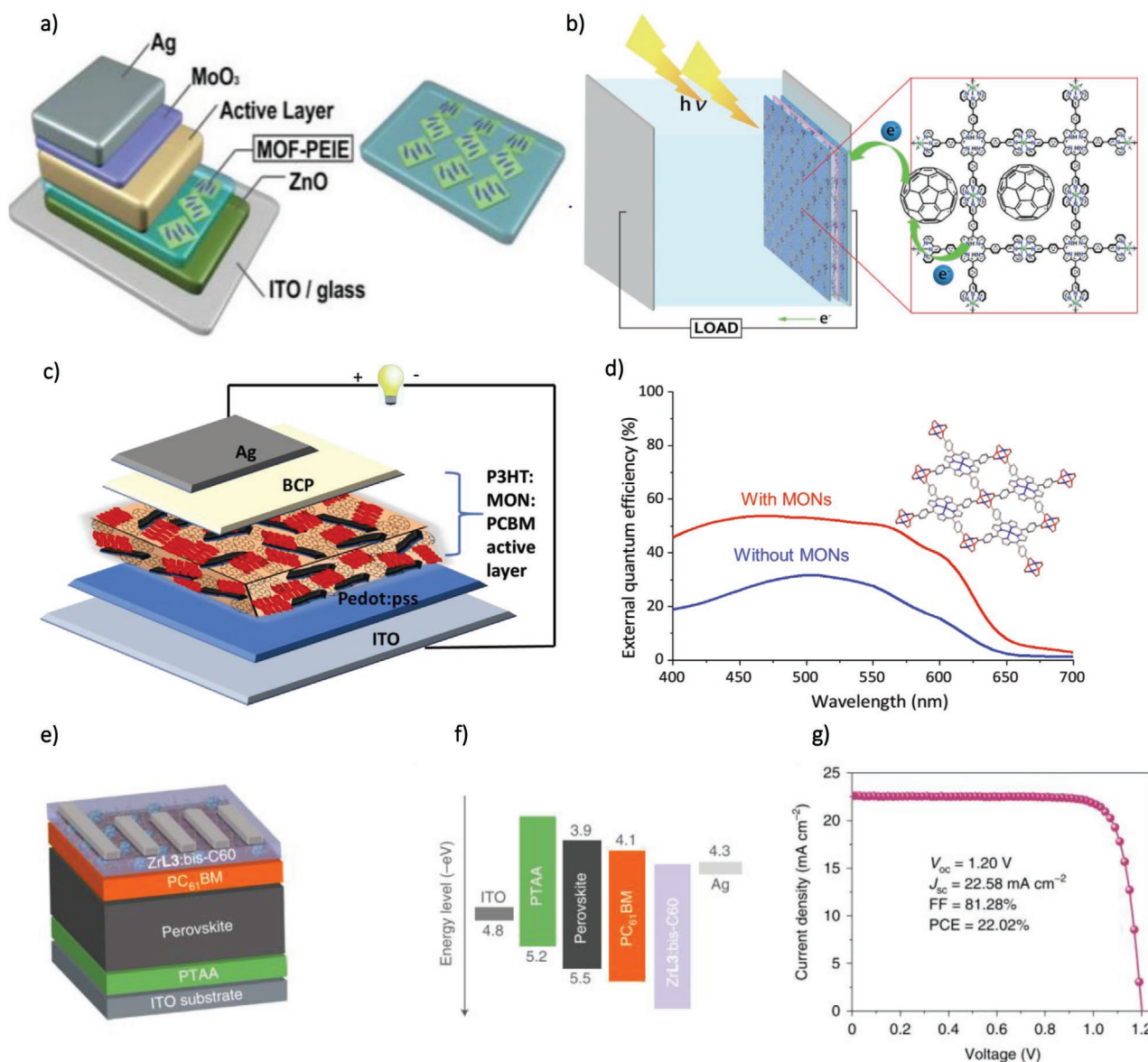
Figure 12. MONs in light harvesting devices. a) Device structure of solar cells investigated with a MON based electron extraction layer. Reproduced with permission.[174] Copyright 2018, Elsevier. b) Schematic representation of the porphyrin based liquid junction solar cell with incorporated fullerene. Reproduced with permission.[177] Copyright 2019, Wiley. c) device structure of solar cells with $Zn_2(ZnTCPP)$ MONs in ternary bulk heterojunctions in our work. d) The external quantum efficiency curves showing enhanced device performance with MONs. c,d) Reproduced with permission.[178] Published by the Royal Society of Chemistry. e) Device structure of the inverted MON based perovskite solar cell; f) the energy level alignment of the used materials in (e); g) The $J–V$ curve of the best performing perovskite solar cell with the MON electron extraction layer. e–g) Reproduced with permission.[179] Copyright 2020, Springer Nature.

devices. While not all MONs are electronically conducting, they are physically flexible enough to stick closely with conductive substrates allowing insulating MONs to be used high performing batteries and supercapacitors. As MONs approach monolayer thicknesses, they offer shorter diffusion paths for the electrons/ions and improve the rate performance. The higher surface area also increases the number of coordinatively unsaturated redox sites leading to higher capacity of the electrodes. The porous nature of MONs is advantageous in the transport of the electrolyte ions in battery applications. MONs also can provide an inert scaffold for psuedocapacitive materials in supercapacitors.

The optical properties of MONs can also be combined with their electronic properties to enable their use in light harvesting and emission applications. MONs have already shown tremendous success in a variety of roles ranging from use as electron extraction layers, to electron donors and light absorbers and emitters. The tunability of MONs also offers great potential for fine-tuning their band-gap in order to optimize overall device performance. The surface chemistry of MONs also allows them to impart morphological changes to devices as well as trap the release of toxic heavy metals and improve the environmental sustainability of devices.

5. Tuneable Porosity and High Anisotropy for Separation Applications

Membrane based separations are of critical importance to enabling a wide range of technologies needed to address the climate emergency including CO_2 capture, hydrogen generation and cleaning polluted water. The suitability of MONs for separation applications stems from the combination of their 2D anisotropic structure, large surface area for separation and inherent porosity provided by the metal-organic structure. MONs therefore possess two distinct routes for mass transport: 1) Through the intrinsic pores within the MON layers 2) by creating a tortuous path for molecules to travel around, differentially interacting with the MONs surfaces as they do so (through both external and interlayer channel mass transport).[180] The diverse and tunable surface chemistry of MONs can allow fine-tuning of interactions with specific molecules, as well as, other components within membranes. The anisotropic structure of MONs allows for their orientation within the membranes, enhancing the tortuous path. At present, it is difficult to compare the performance of different MON-based membranes across the literature, as authors use different feed-pressures, temperatures, substrates, fillers, membrane thickness, and MON loadings (**Table 4**). However, both 2D and MOF materials have already been extensively investigated for separation applications providing a rich literature to build on and compare with. Within this section we discuss how the porosity, anisotropy and tunability of MONs has led to their application in gas separation and water purification applications and highlight significant advances to the state-of-the-art.

5.1. Gas Separation

MON based membranes for gas separation can generally be split into two categories: MON films deposited onto a macroporous support such as α-Al_2O_3, and mixed-matrix membranes (MMMs) in which the MONs are dispersed within a polymer-containing medium and cast into solid membranes. A common problem with incorporating MOFs or other nanoparticle fillers into MMMs is filler agglomeration at relatively low loadings,[181,182] and decreased selectivity due to pathways around the filler because of poor polymer/filler blending.[183] A similar problem occurs for supported films of other 2D materials, in that inefficient packing/stacking of nanosheets exacerbates interlayer channel transport. To avoid this, Yang and co-workers used a hot- drop coating method to deposit a sub-10 µm MON film with disordered nanosheet stacking onto α-Al_2O_3 support instead of the simple filtration common for other 2D materials.[13] This prevented the ordered restacking of MONs into bulk MOF, which would result in blockage of the sieving pores. Jiang et al. took the idea of reducing the non-target diffusion pathway further by including flexible graphene oxide nanosheets into a CuBDC film to "repair" the junctions between MONs, resulting in increased H_2/CO_2 selectivity of 95.1.[184]

Table 4. Summary of data related to CO_2-based gas separations using MONs within the size-discriminative layer.

MON	Layer thickness /µm	s or f, substrate or filler	MON loading /wt%	[a)]Gas pair	Feed conditions p/bar, T/°C	Max. permeance (gas) /GPU	/Barrer	Max. selectivity	Ref.
$[Zn_2(bim)_4]_n$	<0.01	s, α-Al_2O_3	N/A	H_2/CO_2	1, 25	3760 (H_2)	–	291	[13]
$[Zn_2(bim)_3(H_2O)(OH)]_n$	<0.01	s, α-Al_2O_3	N/A	H_2/CO_2	1, 120	2388 (H_2)	–	166	[185]
$[Cu_2(NDC)_2(DABCO)]_n$	40	f, PBI	N/A	H_2/CO_2	5, 35	–	6.13 (H_2)	26.7	[186]
$[Ni_8(5\text{-}BBDC)_6(\mu\text{-}OH)_4]_n$	0.04	s, AAO	N/A	H_2/CO_2	1, 20	553 (H_2)	–	235	[21]
					1, 100	36 (H_2)	–	<8	[21]
$[Cu(BDC)]_n$	47	f, PI	8.2	CO_2/CH_4	7.5, 25	–	2.78 (CO_2)	88.2	[6]
$[Cu(BDC)]_n$		f, PI	12	CO_2/CH_4	20	–	6 (CO_2)	32	[189]
$[Cu(BDC)]_n$	0.66	f, PIM-1	10	CO_2/CH_4	1, 25	407 (CO_2)	–	15.6	[187]
$[Cu(BDC)]_n$	70	f, PIM-1	2	CO_2/CH_4	1, 25	–	2030 (CO_2)	24	[190]
	50	f, 6FDA-DAM	4	CO_2/CH_4	1, 25	–	430 (CO_2)	43	[190]
NUS-8	66	f, PIM-1	2	CO_2/CH_4	1, 25	–	6462 (CO_2)	30.1	[188]
NH_2-MIL-53(Al)	86	f, PI	8	CO_2/CH_4	9, 25	–	11.73 (CO_2)	31.9	[157]
$[Zn(TCPP)]_n$[b)]	0.025	s, PAN	N/A	CO_2/N_2	1, 35	1710 (CO_2)	–	34	[191]
$[Cu(BDC)]_n$[b)]	<0.05	s, Polyactive	N/A	CO_2/N_2 (15/85)	2, 25	129 (CO_2)	–	35	[192]
$[Cu(BDC)]_n$	0.708	f, Polyactive	8	CO_2/N_2 (15/85)	2, 25	40 (CO_2)	–	77	[192]
ZIF-67	<100	f, Pebax	5	CO_2/N_2	1, 25	–	139.4 (CO_2)	73.2	[14]
NUS-8 [...]$_n$	66	f, PIM-1	2	CO_2/N_2	1, 25	–	6725 (CO_2)	26.8	[188]
ZIF-L	unknown	f, Pebax	20	CO_2/N_2 (10/90)	2, 25	–	387.2 (CO_2)	47.1	[193]

[a)]Equimolar unless stated; [b)]MONs are not the sole selective layer in the multilayered membrane; A discriminatory porous polymer layer was additionally present; Acronyms: bim = benzimidazole, NDC = 1,4-naphthalenedicarboxylate, DABCO = 1,4-diazabicyclo[2.2.2]octane, 5-BBDC = 5-*tert*-butyl-1,3-benzenedicarboxylate, MeIM = 5-methylimidazole, PBI = polybenzimidazole, AAO = anodic aluminum oxide, 6FDA-DAM = 4,4′-(hexafluoroisopropylidene)diphthalic anhydride (6FDA) and diaminomesitylene (DAM), PAN = polyacrylonitrile.
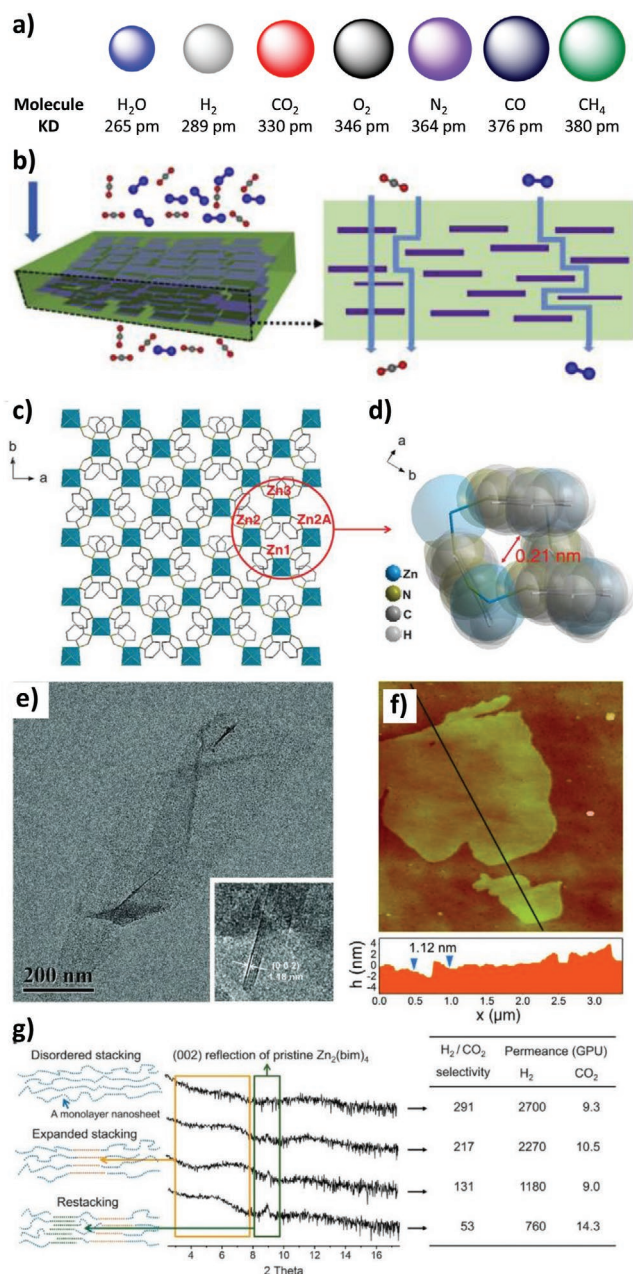
Figure 13. Schematic illustrations of a) different gas molecules' kinetic diameters (KD) and b) mass transport pathways through a MONs. Reproduced with permission.[14] Copyright 2020, Elsevier. c) Illustration of the porous grid-like structure and d) space-filling representation of a pore within a layer of $[Zn_2(bim)_4]_n$. e) TEM and f) AFM images of $[Zn_2(bim)_4]_n$ nanosheets. g) PXRD of membranes with different separation properties with (left) illustrations of microstructural features of the MON layers. c–g) Reproduced with permission.[13] Copyright 2014, AAAS.

For MMMs, Gascon et al. demonstrated that CuBDC nanosheets could be readily included within a polyimide (PI) matrix (**Figure 13**).[6] The high anisotropy of the MONs resulted in near parallel alignment of the MONs within the polymer matrix upon casting into membranes. This was perpendicular to the gas flow direction, readily exposing the pores for the desired gas transport. This led to higher CO_2/CH_4 selectivity

compared to the neat polymer, with difference increasing further upon increasing pressure- the opposite effect to that normally observed for MMMs. This was ascribed to the polymer swelling under increased pressure, reducing the undesirable interlayer channel transport and so increasing the effect of the size-discriminative pathway.

5.1.1. H_2/CO_2 Separations

Separating H_2 from CO_2 relies on the size exclusion of CO_2 (kinetic diameter, KD = 0.33 nm) from H_2 (KD = 0.29 nm) as well as the difference in polarity between the molecules. ZIF-based MONs with relatively small pore apertures are well suited to this separation. Yang's seminal work (**Figure 14**) in 2014 utilized $[Zn_2(bim)_4]_n$ MONs as building blocks for molecular sieving membranes and demonstrated good H_2/CO_2 selectivity of >200 for more than 400 h with a high H_2 permeance up to 3760 gas permeation units (GPU).[13] In practical use, flu gas contains appreciable amounts of H_2O, and so stability under humid conditions at elevated temperature is paramount for uptake of gas separation membranes. These MON films showed good stability over 120 h at 150 °C with a gas feed containing ≈4 mol% steam. Further work developed $[Zn_2(bim)_3(H_2O)(OH)]_n$ films with selectivity up to 166 at elevated temperature.[185]

The Zhao group demonstrated the importance of filler morphology on film separation performance and clearly depicted the importance of using lamellar MONs over bulk MOF crystals and nanoparticles, using polybenzimidazole as the macroporous support.[186] Excitingly, Zhao et al. have also demonstrated the first reversed thermo-switchable MON film, composed of 2D MAMS-1 nanosheets on an anodic aluminum oxide support (**Figure 15**).[21] Normally, gas permeance increases with increasing temperature. However, they found that increasing temperature from room to 100 °C resulted in H_2 permeance decreasing from 392 GPU to merely 14 GPU, and this effect was reversible and repeatable. MAMS-1 has a known thermo-response structure which was expected to increase permeance through increasing aperture size at elevated temperature. Instead, the kinetic opening of the aperture was governed by the rotation of a *tert*-butyl group. At increasing temperature, the free rotation is restricted due to increased steric hindrance resulting from the thermo-responsive structural change, which results in blocking of the pore aperture, and decreased H_2 permeance. This effect could find application in temperature-related gas separations.

5.1.2. CO_2/CH_4 Separations

Separation of CO_2 (KD = 0.33 nm) from CH_4 relies on the size exclusion of larger CH_4 molecules (KD = 0.38 nm). This has been achieved using MMMs of MON and polymers such as, PI, PIM-1, and Pebax. Gascon et al. first incorporated MONs into a MMM for CO_2/CH_4 separation (Figure 13).[6] An 8.2 wt% loading of CuBDC into a polyimide MMM resulted in up to an 80% increase in CO_2 selectivity compared to the control polyimide membrane, and up to an eightfold increase compared

**ADVANCED
SCIENCE NEWS**

www.advancedsciencenews.com

**ADVANCED
FUNCTIONAL
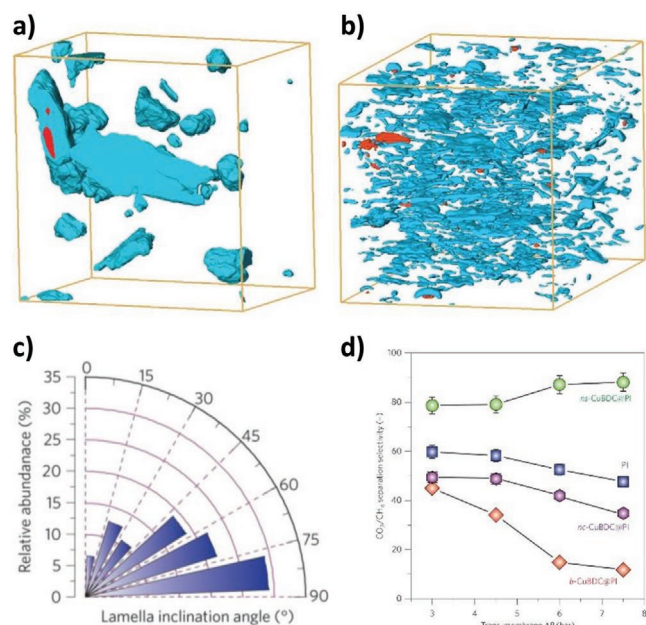MATERIALS**

www.afm-journal.de

Figure 14. Surface-rendered views of segmented FIB-SEM for composite membranes containing a) bulk-type and b) nanosheet CuBDC embedded in PI. MOF particles are shown in blue, while voids are shown in red. Dimensions of box (x:y:z): 11.2:11.2:7.6 a) and 4.9:4.9:6.6 μm b), respectively. c) Angular histogram showing the orientation of MON lamellae with respect to the gas flux direction (y axis) for CuBDC:PI MMM. d) Separation selectivity as a function of the pressure difference over the CuBDC:PI MMM. Data corresponds to steady operation, after >8 h operation, of an equimolar feed of CO_2/CH_4 feed at 298 K. Reproduced with permission.[6] Copyright 2014, Springer Nature.

to bulk MOF MMM. Remarkably, selectivity increased upon increasing upstream pressure. This is contrary to classical polymeric or MOF-MMM membrane operation, due to the polymeric swelling and decreased interlayer transport pathway, discussed in Section 5.1.1.

Zhao and co-workers also used CuBDC but in PIM-1 MMM.[187] They optimized membrane thickness and filler content to achieve a selectivity of 15.6 and CO_2 permeance of 407 GPU, using 10 wt% nanosheet loading and spin coating an ultrathin 660 nm thick MMM (N.B. conventional solution casting typically produces membranes ≈50 μm thick). Increasing membrane thickness increased selectivity, while permeance decreased, consistent with PIM-1 membranes. Introduction of CuBDC nanosheets decreased permeance, and low loadings increased selectivity. MON wt% > 10 resulted in selectivity drop off. The same group also incorporated NUS-8 nanosheets to form a PIM1 MMM.[188] In this case, a 2 wt% loading of MONs was the maximum achievable before noticeable agglomeration within the MMM and subsequent negative property introduction. The authors demonstrated that there was good interaction between the large surface area of NUS-8 MONs and PIM-1, through π-π interactions and H-bonding. This led to an increase in polymer chain packing (i.e., increase in crystallinity) in the MMM, beneficial to gas separation through increasing the discriminative diffusion pathway through the MONs.

Tsapatsis et al. incorporated 12 wt% CuBDC MONs into a polyimide MMM which resulted in a 70% increase in selectivity compared to the pure PI membrane.[189] Interestingly, they applied a mathematical model for flake composites based on their own and Gascon's previous data,[6] to predict the performance of other literature MMMs. Model predictions for other fillers were an
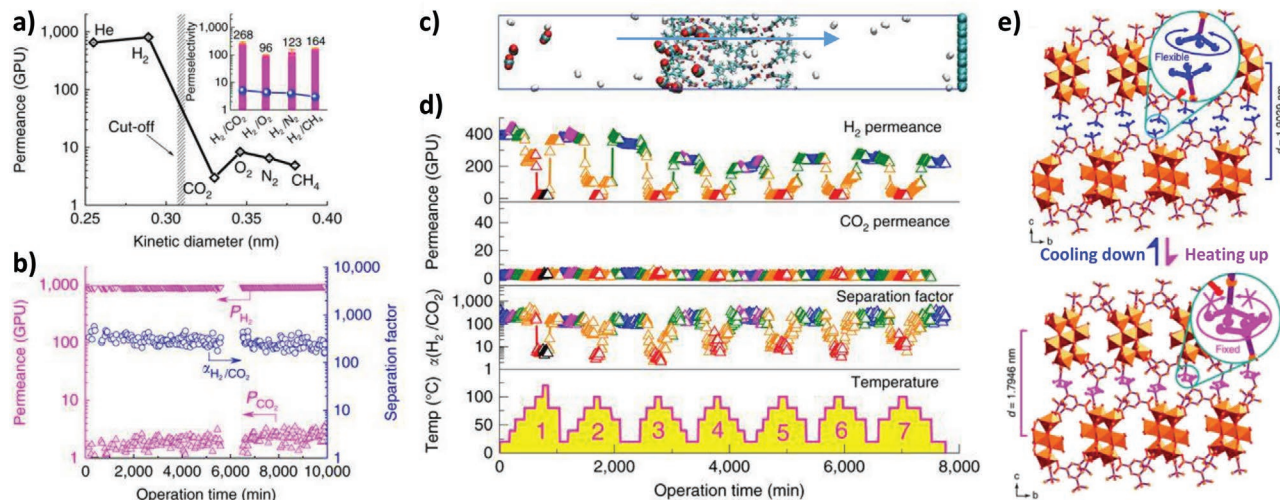

Figure 15. a) Single gas permeation of the membrane (blue line in insert figure indicates the Knudsen diffusion selectivity of H_2 over other gases). b) A 10 000 min continuous test of the membrane for the separation of equimolar H_2/CO_2 mixture at room temperature. c) A snapshot of molecular dynamics simulation for the separation of equimolar H_2/CO_2 mixture through a bilayered MAMS-1 membrane (after 80 ns of simulation). d) Gas permeance and H_2/CO_2 separation factors of the 40-nm membrane under seven heating/cooling cycles. Different colors represent various temperatures: Blue, 20 °C; magenta, 40 °C; olive, 60 °C; orange, 80 °C; red, 100 °C; and black, 120 °C. e) Illustration of shrinkage and expansion upon heating and cooling, respectively, on interlayer distance of MAMS-1, with freely rotating and "frozen" *tert*-butyl groups highlighted in blue and magenta, respectively. Adapted with permission.[21] Copyright 2017, Springer Nature.

**ADVANCED
SCIENCE NEWS**

www.advancedsciencenews.com

**ADVANCED
FUNCTIONAL
MATERIALS**

www.afm-journal.de

order of magnitude lower than the observed CO_2 permeability, which the authors ascribe to non-selective interlayer channel transport not considered in the model. Nonetheless, modelling of gas transport pathways is an interesting development in which there is scope for improvement as the blending of MONs and polymers become increasingly understood.

Gascon et al. more recently demonstrated a synthetic route to MONs of non-layered frameworks, using CTAB polymer surfactant to adsorb selectively to a crystal face within the MOF synthesis, resulting in free-standing lamellae of non-layered Al-based MONs, which have 1D channels.[157] Incorporating 8 wt% of these MONs into a polyimide MMM resulted in maintenance of the CO_2 selectivity, while nearly doubling the permeance.

5.1.3. CO_2/N_2 Separations

Separation of CO_2 (KD = 0.33 nm) from N_2 relies on the size exclusion of the larger N_2 (KD = 0.36 nm). Qiao et al. used relatively large pore ZnTCPP (pore size ≈1.27 nm) film as an intermediary highly permeable gutter layer in a composite membrane.[191] This layer can prevent the polymer solution penetrating into the porous support, which is a common problem with low concentrations of polymer used to make ultrathin membranes. The introduction of the MON gutter layer increased permeability to ≈2100 GPU whilst maintaining the selectivity of the membrane around 30, which satisfied the properties desired in for an economically viable post-combustion CO_2 capture membrane.

Kapteijn and co-workers incorporated CuBDC MONs as a gutter layer within a composite membrane and found that this was more beneficial to membrane performance than a classical poly(dimethylsiloxane) gutter layer.[192] The main role of the MONs was to cover the defects in the thin films. They also manufactured MMMs containing CuBDC MONs. Supporting these on polyacrylonitrile porous supports further increased the CO_2 selectivity (77 v 60 for free standing MMMs).

Water stability is an important factor to consider when using MONs within membranes for gas separation. Sun and co-workers incorporated ZIF-67, [Co(methylimidazole)]$_n$, pore size ≈0.34 nm) MONs in Pebax (polyether block amide MH 1657) MMMs.[14] ZIF-67 is a non-layered structure, but their synthetic method promoted growth in the [211] direction. The hydrothermal stability of ZIF-67 was improved through the morphology regulation, due to fewer exposed Co–N bonds per unit area on the exposed crystal faces. MON/Pebax MMM showed improved permeability (139.4 barrer, 50.7% increase) and ideal selectivity (73.2, 76% increase) with a 5 wt% loading compared to pure Pebax membranes.

5.2. Water Purification

5.2.1. Organics

The impending worldwide clean water crisis means that developing new water purification techniques is becoming increasingly pressing.[197] Ang and Hong published the first example of nanofiltration from aqueous solution in 2017.[28] They cross linked the terminal carboxylate groups of mixed metal TCPP-based

MONs with polycationic polymer to form the selective layer within a nanofiltration membrane. Water flux was 4243 L m^{-2} h^{-1} bar^{-1} at a low pressure of 0.01 bar, with good rejection rates (90%) for dyes (size ≈ 0.8 × 1.1 nm) and salt (20–40%). The separation performance at low pressure was a record at the time, and surpassed equivalent graphene or graphene-oxide based membranes. A GO membrane minimum operational pressure was 0.56 bar. The reduced pressure required for MON based membranes was explained by the transport pathway through the pores of the framework, which graphene-based nanosheets do not possess. Similarly, the water flux was double that of the control polymer-based membrane. Peng et al. have also crosslinked their $[Zn_2(bim)_3(OH)(H_2O)]_n$ MONs, with poly(amidoamine) dendrimers, to enhance the interlayer interactions and stabilize the nanosheet stacking in water (**Figure 16**b).[194] Crosslinking
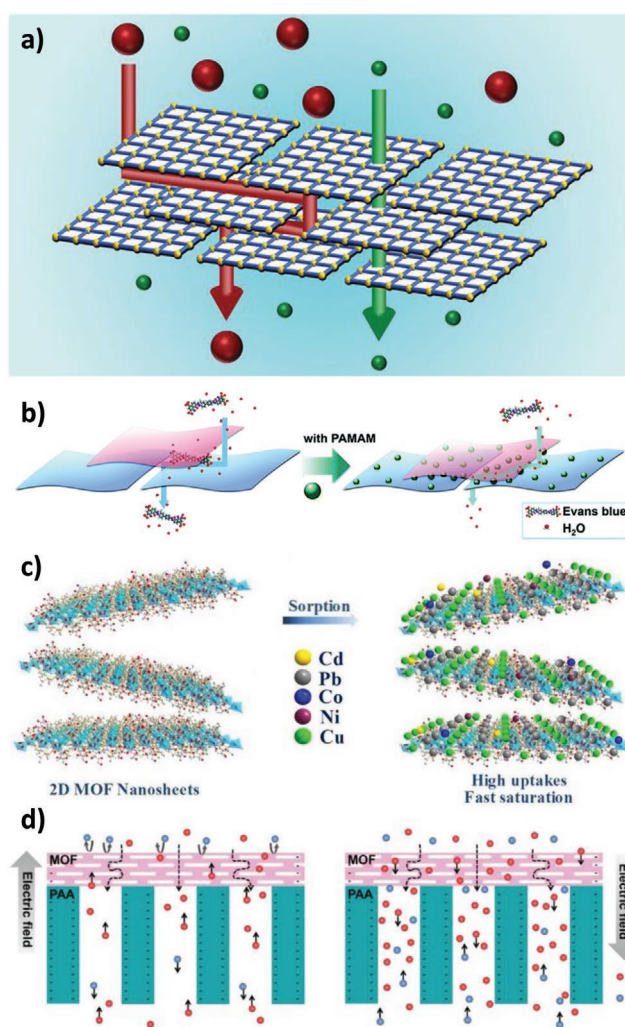

Figure 16. Schematics of methods of water purification: a) General scheme of mass transport pathway through a MON film membrane. Reproduced with permission.[41] Copyright 2019, Wiley. b) The improved selectivity when cross-linking nanosheets. Reproduced with permission.[194] Copyright 2019, Royal Society of Chemistry. c) Heavy metal ion adsorption to MON. Reproduced with permission.[195] Copyright 2020, Elsevier. d) Illustration of the "off" (left) state in the ion current rectification, which results from ion concentration depletion in the nanochannels, and "on" (right) state. Reproduced with permission.[196] Copyright 2019, Wiley.

**ADVANCED
SCIENCE NEWS**

www.advancedsciencenews.com

**ADVANCED
FUNCTIONAL
MATERIALS**

www.afm-journal.de

endowed the membrane with antiswelling character when exposed to water, and resulted in markedly improved dye (Evans blue, 1.2×3.1 nm^2) rejection rate (99.4%) compared to a pristine non-crosslinked MON membrane.

Gao et al. used layered lanthanide-based [Eu(BTB)(H$_2$O)$_2$.solvent]$_n$ nanosheets (5 wt%) with 1D channel pores in a sodium alginate membrane for the dehydration of ethanol.[198] Both ethanol and water fit through the 1D channel (0.5–0.8 nm diameter), but the hydrophobic internal environment means there is a large energy barrier to ethanol transport. Water molecules are significantly smaller and so can pass through the channels much more easily, resulting in a large water flux (1996 g m^{-2} h^{-1}) and high selectivity for H$_2$O (1160) from a 10 wt% water in ethanol solution.

5.2.2. Oil/Water Separations

Deng et al. prepared hydrophobic MONs and demonstrated their use in separating oil from water.[199] A post-synthetic modification technique was used to exchange pillaring bipyridine in the 3D-connected MOF with monotopic substituted pyridine derivatives, which resulted in exfoliation to form MONs. The subsequent presentation of the hydrophobic groups of the substituted pyridine derivatives on the exposed surfaces of the MONs enabled the efficient separation of oils (cyclohexane or dichloroethane) from water using a column packed with MONs. When the original 3D-connected MOF was used, both oils and water readily passed through.

5.2.3. Desalination and Ion Separation

The reduced dimensions of MON based membranes holds particular promise in increasing the permeability of membranes in desalination applications. Wang and co-workers used CuBDC MONs (pore aperture 0.52 nm) to improve polyamide membrane performance in forward osmosis, increasing water permeability by 61% compared to the pristine membrane, while decreasing salt permeability by 24% (hydrated ion diameter = 0.42 and 0.66 nm for Na$^+$ and Cl$^-$, respectively). The inclusion of CuBDC nanosheets also contributed to increased antifouling behaviour using municipal wastewater. This was attributed to multiple effects including the increased hydrophilicity of the membrane surface, which facilitates the formation of a thin water film at the water-membrane interface and serves as a barrier against foulant adhesion. However, increased dead bacteria cells were observed for the CuBDC membrane, suggesting biocidal properties that may result from Cu^{2+} leaching from the membrane.[200]

Farimani et al. used molecular dynamic simulation to suggest that hexaaminobenzene-based MONs[18] of over two layers thick may successfully reject almost 100% of Na$^+$ and Cl$^-$ ions.[201] Peak water permeation of two-layer MONs was an order of magnitude larger than that of graphene or MoS$_2$, and was between 3 and 6 orders of magnitude larger permeation than commercially used membranes. This assumes a "perfect" crystalline membrane, which is not achievable in practise, nonetheless this work suggests that MON may have a good future within desalination membranes.

Recently, Wang et al. demonstrated that a layer of CuTCPP(Fe) grown over porous anodic aluminum could be used a nanochannel mimic for biological ion channel (K$^+$ and Cl$^-$).[196] A power density of 1.6 W m^2 was achieved by integrating this into a salinity-gradient-driven energy conversion device. Further improvements to such nanofluidic devices could be made through strategies such as surface modification and tuning MON film thickness.

5.2.4. Heavy Metal Adsorption

An alternative method of water remediation is chemical adsorption, typically using porous adsorbents. This is advantageous due to simplicity and cost efficiency.[202] New porous materials such as MOFs, COFs and porous organic polymers are emerging as a burgeoning class of adsorbents; however, buried chelating sites still limit full accessibility. Wang et al. used MONs containing thiocyanate groups for mercury chloride capture from aqueous solution.[203] The maximum uptake was 1698 mg g^{-1}, and the adsorption had very fast kinetics (reducing mercury concentration from 10 ppm to 1 ppb within 15 min), attributed to the total exposure of chelating sites on the surfaces of the MONs. Moreover, building blocks of 2D Hg-MON produced a new 3D framework with permanent porosity through stacking of layers with adsorbed Hg. Duan et al. showed that exposed C—N(H) and O—H groups could complex U^{6+} in a exothermic and spontaneous nature, in solution.[204] Similarly, Xu et al. used MONs with exposed imino and hydroxyl groups to selectively adsorb Pb^{2+} and Cu^{2+} ions, respectively, from a solution containing other heavy metals (Figure 16c).[195] Facile access to adsorbing sites on the MON surface resulted in fast adsorption kinetics, with saturation occurring within 90 and 30 min for Pb^{2+} and Cu^{2+} and maximum loadings of 253.8 and 335.6 mg g^{-1}, respectively. Metal sites are coordinatively saturated within this framework structure, therefore outer-sphere surface complexes dominated the metal adsorption mechanism.

5.2.5. Nanoparticle Sieving

The regular nanochannels presented by MONs could render them useful in nanoparticle sieving applications, where there is specific size requirements for the particles utilized. Ruoff and co-workers utilized [Cu$_3$(tri(β-diketone)$_2$)]$_n$ MONs with pore size = 0.45 nm (by N$_2$ adsorption) to form a 50 μm thick film supported on an Anodisc membrane support (pore size = 0.02 μm).[205] They demonstrated that this could effectively sieve Au NPs with diameter > 2.4 nm from a mixture with (average ± standard deviation) diameters 1.4 ± 0.8 nm. The transport pathway of the NPs in this study is unclear, however the effective use of MON frameworks with different effective pore sizes could allow this approach to be tailored towards the selection of different size distributions of NPs.

5.3. Perspective

Many of the earliest and highest profile applications of MONs are in the area of separation, likely because the use of MOFs

**ADVANCED
SCIENCE NEWS**

www.advancedsciencenews.com

**ADVANCED
FUNCTIONAL
MATERIALS**

www.afm-journal.de

for gas storage and separation is so well established. MONs have already demonstrated clear advantages over their bulk counter parts, with several examples showing how the nanoscopic dimensions of MONs can reduce membrane thickness leading to increased permeability and selectivity. MONs have been used to separate species across a range of length scales from hydrogen molecules to nanoparticles. This is in part because MONs have well defined, crystalline structures, which allows their pore size and chemistry to be precisely tuned. Judicial combination of ligand and SBU allow control over aperture sizes, for example, ≈ 0.21 nm for benzimidazole based $[Zn_2(bim)_4]_n$,[13] and ≈ 2.3 nm for quaterphenyldicarboxylate based MONs.[117] MOFs with apertures up to ≈ 10 nm have previously been synthesized indicating the potential to extend this range even further. The tunable chemistry of the MONs pores is equally important in determining selectivity as shown, for example, by the ability of hydrophobic pores to pass larger oil molecules but not water. It is likely that many of the systems and techniques that have been developed for gas storage and separation in MOFs will apply equally in enhancing the selectivity of MON based membranes. Similarly, there are a number of industrially relevant gas-pair separations that have received attention using MOFs, such as H_2/C_3H_8, C_2H_4/C_2H_6, and $C_3H_6/C_3H_8$217 and therefore there is significant scope for developing MONs towards these applications.[206] However, there are also likely to be significant differences in the mechanisms by which molecules diffuse through MON based membranes due to the ultrashort through pore distances and detailed experimental and theoretical studies to understand this would be of great interest.

Like other 2D materials, the anisotropic structure of MONs means they create a tortuous path forcing molecules to interact with functional groups on their surfaces. The size of the nanosheets used in the studies varies considerably from a few hundred nanometers to microns wide and from a single layer to more than 50 layers thick. At this stage, it is not clear what the optimal size of nanosheet is and studies comparing the same nanosheets with different aspect ratios would be highly beneficial. All of the MONs investigated to date have a relatively simple structure and there is plenty of scope for designing ligands, metal-clusters, and post-synthetic functionalization to create more targeted interactions with specific analytes. Compared to bulk fillers, 2D materials have very large external surfaces that exacerbate the importance of interactions between the MONs and other components present. Optimizing MON-polymer interaction is therefore equally important and indeed the effect of the MONs are sometimes amplified through ordering the surrounding polymer, leading to increased selectivity. The antifouling properties of MONs due to the release of metal ions is another potential benefit of using MONs in water-separation applications, although it also raises questions regarding their long-term stability and potential for use in, for example, generating potable water where the potential release of metal-ions and ligands raises potential health or environmental concerns. Overall, although further optimization and understanding is required before uptake for large-scale separations, MONs have great promise for utilization across separation applications.

6. Overall Perspective and Outlook

The growing body of research on MONs has already demonstrated how the distinct combination of properties they offer allow them to be exploited in a diverse range of applications. The high external surface area and periodic structure of MONs creates a high density of accessible active sites. This has been exploited extensively in catalysis with MONs showing increased rates of reaction compared to their bulk counterparts, as well as, to a lesser degree in sensing to enhance sensitivity and response times. The anisotropic structure of MONs helps orientate MONs within membranes and combined with their high surface area create "tortuous paths" for separation applications. Their ultrathin dimensions and intrinsic porosity also open a second route by which some molecules, but not others, can pass through MONs. This combination of high external surface area and intrinsic porosity is also central to their success in many electronics applications where close contact with electrolytes and ion mobility are key.

It is the diverse chemistry and programmable structures of MONs that most distinguishes them from other 2D materials and has enabled their use in such a range of applications. Metal ions and clusters have been used as Lewis acidic sites in catalytic, sensing and separation applications. Metals can also provide MONs with advantageous optical and electronic properties such as long-lived fluorescence, metal-to-ligand charge transfer, semi-conducting behaviour, magnetism, and redox activity, which have been extensively exploited. The molecular nature of MONs allows for fine-tuning of their structure and properties and for new functionalities to be added without disrupting their 2D connectivity.

Of the >88 000 crystal structures contained in the MOF subset of the Cambridge Structural Database (MOF-CSD), one third are estimated to be layered providing a wealth of materials that could be exfoliated to form MONs.[207] However, despite the almost infinite number of potential MONs that could be made, most application papers draw on a handful of previously reported structures. This is presumably testament to the challenges in optimizing new MON systems with those working on applications preferring (not unreasonably) to make use of established systems. It is interesting to note that many of the structures that appear repeatedly in this review have close analogues to the 3D architectures that dominate much of the MOF literature, particularly HKUST-1, UIO-66, and ZIF-8. Clearly these robust, accessible, neutral architectures work well but at this early stage it is far from clear that the rules that govern the design of 3D MOFs will be optimal for 2D materials. There is therefore considerable work still to be done in understanding the fundamental design principles behind MONs in order to create new architectures with potentially improved dimensions and properties. In particular, MONs with conducting, semi-conducting and redox active SBU's would be valuable for use in variety of catalytic, sensing and electronics applications.

In addition to the properties of the ligands and metal ions that make up the structural backbone of the MONs, active components have been added to the surface of MONs through post-synthetic modification. This approach overcomes many of

**ADVANCED
SCIENCE NEWS**

www.advancedsciencenews.com

**ADVANCED
FUNCTIONAL
MATERIALS**

www.afm-journal.de

the challenges of developing new systems and allows for the introduction of active components not compatible with the synthetic conditions or that would disrupt nanosheet formation. In contrast to most other 2D materials, the periodic structure of MONs means that groups are introduced in well-defined positions with respect to each other. The potential of this approach is perhaps best demonstrated in some of the sophisticated photocatalytic systems developed by Lin, Wang and co-workers where Zr/Hf MONs are used as scaffolds to co-ordinate multiple different light absorbing and catalytic groups with respect to each other.

Another trend that repeats across this review is the use of MONs as just one component within often complex mixtures that form a functional system. Examples range from the use of MONs as fluorescence quenchers in enzyme-based glucose sensors, as a scaffold to separate faradaic nanoparticles within supercapacitors, and as additives with solar cells or mixed matrix membranes. Here the other components can make up for potential deficiencies in the MONs properties such as a lack of selectivity, conductivity or structural stability. The high surface area of MONs enables them to interact strongly with other components within the mixtures and even small quantities can have a templating effect on surrounding components amplifying their properties. The monolayer dimensions of ultrathin MONs allow for efficient transfer of excited states and charges to-and-from other components within blends.

The scalable synthesis of ultrathin MONs with high aspect ratios in good yields is an outstanding problem in the field. Other reviews provide a good discussion of the range of methods that have so far been used to synthesis MONs and the relative advantages and disadvantages of each approach. It is worth highlighting here that the optimal method will vary for each application depending on the desired characteristics of the MONs. For example, surfactant-assisted synthesis routes can offer improved aspect ratios and yields, but the surfactants can be difficult to remove and potentially block active sites on the surfaces of MONs inhibiting their use in catalysis or sensing applications. Monolayer thickness and well-defined lateral dimensions may be essential for some applications, but in others it might be more economic to accept a broader particle size distribution in order to achieve a higher yield of material. Fabricating nanosheets with large lateral dimensions is typically more challenging and having micron-sized nanosheets may be beneficial in, for example, forming free standing membranes. However, large lateral dimensions may be undesirable in other applications such as thin films, composite blends or where stable suspensions need to be formed. Systematic studies are required to understand the effect of different particle size distribution on performance and compare the same MONs prepared using different methods to identify the best approach for each application.

In comparison to many inorganic 2D materials formed using covalent or ionic bonds, the molecular nature and relatively labile co-ordination bonds of MONs mean they typically have lower thermal stabilities and are less resistant to attack by reactive chemical species. The potential for decomposition or structural rearrangements highlights the importance of fully characterizing systems before and after function. However, the articles in this review indicate that despite their apparent fragility,

MONs can be designed which are remarkably robust and survive in a wide range of solvents, biological fluids, when irradiated with light, strong electric fields and high ionic concentrations. Showing the stability and recyclability of MONs persists during long-term testing under real world conditions is a key them finding use in real-world applications.

The intense academic and industrial interest in both 2D and MOF materials over the last two decades highlights the potential for MONs as a class of materials which combines the properties of both. This review highlights the inroads that have already been made over just the last five years in exploring the potential of MONs for use within catalysis, sensing, electronics and separation applications. We anticipate that next five years will continue to see an exponential growth in research on MONs as new materials and methods are developed, existing systems are further functionalised and optimized, the role of MONs within existing applications is better understood and new opportunities investigated.

Conflict of Interest

The authors declare no conflict of interest.

Author Contributions

R.R.R.P., K.S. and D.J.A. were lead authors of sections 2, 4 and 5 respectively. JN was the lead author of section 3 and edited the whole manuscript together. J.A.F. contributed to all sections and editing of the manuscript.

[1] M. Zhao, Y. Huang, Y. Peng, Z. Huang, Q. Ma, H. Zhang, *Chem. Soc. Rev.* **2018**, *47*, 6267.

[2] D. J. Ashworth, J. A. Foster, *J. Mater. Chem. A* **2018**, *6*, 16292.

[3] S. R. Batten, N. R. Champness, X. M. Chen, J. Garcia-Martinez, S. Kitagawa, L. Öhrström, M. O'Keeffe, M. P. Suh, J. Reedijk, *CrystEngComm* **2012**, *14*, 3001.

[4] M. J. Kalmutzki, N. Hanikel, O. M. Yaghi, *Sci. Adv.* **2018**, *4*, eaat9180.

[5] Z. Q. Li, L. G. Qiu, W. Wang, T. Xu, Y. Wu, X. Jiang, *Inorg. Chem. Commun.* **2008**, *11*, 1375.

[6] T. Rodenas, I. Luz, G. Prieto, B. Seoane, H. Miro, A. Corma, F. Kapteijn, F. X. L. I. Xamena, J. Gascon, *Nat. Mater.* **2015**, *14*, 48.

**ADVANCED
SCIENCE NEWS**
www.advancedsciencenews.com

**ADVANCED
FUNCTIONAL
MATERIALS**
www.afm-journal.de

[7] J. A. Foster, S. Henke, A. Schneemann, R. A. Fischer, A. K. Cheetham, *Chem. Commun.* **2016**, *52*, 10474.

[8] Z. Hu, E. M. Mahdi, Y. Peng, Y. Qian, B. Zhang, N. Yan, D. Yuan, J. C. Tan, D. Zhao, *J. Mater. Chem. A* **2017**, *5*, 8954.

[9] L. Cao, Z. Lin, W. Shi, Z. Wang, C. Zhang, X. Hu, C. Wang, W. Lin, *J. Am. Chem. Soc.* **2017**, *139*, 7020.

[10] Z. Lin, N. C. Thacker, T. Sawano, T. Drake, P. Ji, G. Lan, L. Cao, S. Liu, C. Wang, W. Lin, *Chem. Sci.* **2017**, *9*, 143.

[11] M. J. Cliffe, E. Castillo-Martínez, Y. Wu, J. Lee, A. C. Forse, F. C. N. Firth, P. Z. Moghadam, D. Fairen-Jimenez, M. W. Gaultois, J. A. Hill, O. V. Magdysyuk, B. Slater, A. L. Goodwin, C. P. Grey, *J. Am. Chem. Soc.* **2017**, *139*, 5397.

[12] S. C. Junggeburth, L. Diehl, S. Werner, V. Duppel, W. Sigle, B. V. Lotsch, *J. Am. Chem. Soc.* **2013**, *135*, 6157.

[13] Y. Peng, Y. Li, Y. Ban, H. Jin, W. Jiao, X. Liu, W. Yang, Y. Peng, Y. Li, Y. Ban, H. Jin, W. Jiao, X. Liu, W. Yang, Y. Peng, Y. Li, B. Yujie, H. Jin, W. Jiao, X. Liu, W. Yang, *Science* **2014**, *346*, 1356.

[14] S. Feng, M. Bu, J. Pang, W. Fan, L. Fan, H. Zhao, G. Yang, H. Guo, G. Kong, H. Sun, Z. Kang, D. Sun, *J. Membr. Sci.* **2020**, *593*, 117404.

[15] T. Kambe, R. Sakamoto, K. Hoshiko, K. Takada, M. Miyachi, J. H. Ryu, S. Sasaki, J. Kim, K. Nakazato, M. Takata, H. Nishihara, *J. Am. Chem. Soc.* **2013**, *135*, 2462.

[16] D. Sheberla, L. Sun, M. A. Blood-Forsythe, S. Er, C. R. Wade, C. K. Brozek, A. Aspuru-Guzik, M. Dincă, *J. Am. Chem. Soc.* **2014**, *136*, 8859.

[17] A. J. Clough, J. W. Yoo, M. H. Mecklenburg, S. C. Marinescu, *J. Am. Chem. Soc.* **2015**, *137*, 118.

[18] N. Lahiri, N. Lotfizadeh, R. Tsuchikawa, V. V. Deshpande, J. Louie, *J. Am. Chem. Soc.* **2017**, *139*, 19.

[19] P.-Z. Li, Y. Maeda, Q. Xu, *Chem. Commun.* **2011**, *47*, 8436.

[20] Q. Qiu, H. Chen, Z. You, Y. Feng, X. Wang, Y. Wang, Y. Ying, *ACS Appl. Mater. Interfaces* **2020**, *12*, 5429.

[21] X. Wang, C. Chi, K. Zhang, Y. Qian, K. M. Gupta, Z. Kang, J. Jiang, D. Zhao, *Nat. Commun.* **2017**, *8*, 14460.

[22] A. Abhervé, S. Mañas-Valero, M. Clemente-León, E. Coronado, *Chem. Sci.* **2015**, *6*, 4665.

[23] J. López-Cabrelles, S. Mañas-Valero, I. J. Vitórica-Yrezábal, P. J. Bereciartua, J. A. Rodríguez-Velamazán, J. C. Waerenborgh, B. J. C. Vieira, D. Davidovikj, P. G. Steeneken, H. S. J. van der Zant, G. M. Espallargas, E. Coronado, *Nat. Chem.* **2018**, *10*, 1001.

[24] J. Xie, Y. Wang, D. Zhang, C. Liang, W. Liu, Y. Chong, X. Yin, Y. Zhang, D. Gui, L. Chen, W. Tong, Z. Liu, J. Diwu, Z. Chai, S. Wang, *Chem. Commun.* **2019**, *55*, 11715.

[25] J. Huang, Y. Li, R. K. Huang, C. T. He, L. Gong, Q. Hu, L. Wang, Y. T. Xu, X. Y. Tian, S. Y. Liu, Z. M. Ye, F. Wang, D. D. Zhou, W. X. Zhang, J. P. Zhang, *Angew. Chem., Int. Ed.* **2018**, *57*, 4632.

[26] Y. Ding, Y. P. Chen, X. Zhang, L. Chen, Z. Dong, H. L. Jiang, H. Xu, H. C. Zhou, *J. Am. Chem. Soc.* **2017**, *139*, 9136.

[27] L. Cao, Z. Lin, F. Peng, W. Wang, R. Huang, C. Wang, J. Yan, J. Liang, Z. Zhang, T. Zhang, L. Long, J. Sun, W. Lin, *Angew. Chem., Int. Ed.* **2016**, *55*, 4962.

[28] H. Ang, L. Hong, *ACS Appl. Mater. Interfaces* **2017**, *9*, 28079.

[29] G. Xu, K. Otsubo, T. Yamada, S. Sakaida, H. Kitagawa, *J. Am. Chem. Soc.* **2013**, *135*, 7438.

[30] R. Sakamoto, K. Hoshiko, Q. Liu, T. Yagi, T. Nagayama, S. Kusaka, M. Tsuchiya, Y. Kitagawa, W. Y. Wong, H. Nishihara, *Nat. Commun.* **2015**, *6*, 6713.

[31] B. Wang, J. Shang, C. Guo, J. Zhang, F. Zhu, A. Han, J. Liu, *Small* **2019**, *15*, e1804761.

[32] L. Zhuang, L. Ge, H. Liu, Z. Jiang, Y. Jia, Z. Li, D. Yang, R. K. Hocking, M. Li, L. Zhang, X. Wang, X. Yao, Z. Zhu, *Angew. Chem.* **2019**, *131*, 13699.

[33] R. Sakamoto, K. Takada, T. Pal, H. Maeda, T. Kambe, H. Nishihara, *Chem. Commun.* **2017**, *53*, 5781.

[34] J. Duan, Y. Li, Y. Pan, N. Behera, W. Jin, *Coord. Chem. Rev.* **2019**, *395*, 25.

[35] C. Tan, X. Cao, X. J. Wu, Q. He, J. Yang, X. Zhang, J. Chen, W. Zhao, S. Han, G. H. Nam, M. Sindoro, H. Zhang, *Chem. Rev.* **2017**, *117*, 6225.

[36] T. Hyun, J. Jeong, A. Chae, Y. K. Kim, D.-Y. Koh, *BMC Chem. Eng.* **2019**, *1*, 12.

[37] M. A. Solomos, F. J. Claire, T. J. Kempa, *J. Mater. Chem. A* **2019**, *7*, 23537.

[38] S. Kim, H. Wang, Y. M. Lee, *Angew. Chem., Int. Ed.* **2019**, *58*, 2.

[39] G. Chakraborty, I.-H. Park, R. Medishetty, J. J. Vittal, *Chem. Rev.* **2021**, *121*, 3751.

[40] W. Zhao, J. Peng, W. Wang, S. Liu, Q. Zhao, W. Huang, *Coord. Chem. Rev.* **2018**, *377*, 44.

[41] Y. Peng, W. Yang, *Adv. Mater. Interfaces* **2019**, *7*, 1901514.

[42] A. Dhakshinamoorthy, A. M. Asiri, H. Garcia, *Adv. Mater.* **2019**, *31*, 1900617.

[43] M. Xu, S. S. Yang, Z.-Y. Gu, *Chem. – Eur. J.* **2018**, *24*, 15131.

[44] D. Zhu, M. Qiao, J. Liu, T. Tao, C. Guo, *J. Mater. Chem. A* **2020**, *8*, 8143.

[45] Y. N. Li, S. Wang, Y. Zhou, X. J. Bai, G. S. Song, X. Y. Zhao, T. Q. Wang, X. Qi, X. M. Zhang, Y. Fu, *Langmuir* **2017**, *33*, 1060.

[46] B. Wang, J. Jin, B. Ding, X. Han, A. Han, J. Liu, *Front. Mater.* **2020**, *7*, 37.

[47] F. Zhang, J. Zhang, B. Zhang, L. Zheng, X. Cheng, Q. Wan, B. Han, J. Zhang, *Nat. Commun.* **2020**, *11*, 1431.

[48] X. Zhang, L. Chang, Z. Yang, Y. Shi, C. Long, J. Han, B. Zhang, X. Qiu, G. Li, Z. Tang, *Nano Res.* **2019**, *12*, 437.

[49] X. Yang, R. Xiong, X. Chang, S. Wang, Z. Ding, Q. Li, *ChemistrySelect* **2019**, *4*, 14300.

[50] Y. Xiao, W. Guo, H. Chen, H. Li, X. Xu, P. Wu, Y. Shen, B. Zheng, F. Huo, W. D. Wei, *Mater. Chem. Front.* **2019**, *3*, 1580.

[51] S. Wang, T. Wang, H. Zheng, F. Fan, Z. Gu, W. He, B. Zhang, L. Shao, H. Chen, Y. Li, X. Zhang, L. Zhang, Y. Fu, W. Qi, *Microporous Mesoporous Mater.* **2020**, *303*, 110254.

[52] J. Wang, J. Zhang, S. B. Peh, L. Zhai, Y. Ying, G. Liu, Y. Cheng, D. Zhao, *ACS Appl. Energy Mater.* **2019**, *2*, 298.

[53] Y. Hu, Y. Zhang, Y. Han, D. Sheng, D. Shan, X. Liu, A. Cheng, *ACS Appl. Nano Mater.* **2019**, *2*, 136.

[54] W. Shi, L. Zeng, L. Cao, Y. Huang, C. Wang, W. Lin, *Nano Res.* **2020**, *14*, 473.

[55] C. Tan, K. Yang, J. Dong, Y. Liu, Y. Liu, J. Jiang, Y. Cui, *J. Am. Chem. Soc.* **2019**, *141*, 17685.

[56] J. Nicks, J. Zhang, J. A. Foster, *Chem. Commun.* **2019**, *55*, 8788.

[57] R. Yan, Y. Zhao, H. Yang, X. J. Kang, C. Wang, L. L. Wen, Z. D. Lu, *Adv. Funct. Mater.* **2018**, *28*, 1802021.

[58] G. Zhan, H. C. Zeng, *Adv. Funct. Mater.* **2016**, *26*, 3268.

[59] J. Liu, H. Yu, L. Wang, *Appl. Catal., A* **2020**, *599*, 117605.

[60] S. Wu, L. Qin, K. Zhang, Z. Xin, S. Zhao, *RSC Adv.* **2019**, *9*, 9386.

[61] T. Guo, C. Wang, N. Zhang, Y. Zhang, T. Chen, X. Xing, Z. Lu, L. Wen, *Cryst. Growth Des.* **2020**, *20*, 6217.

[62] X. Zhang, P. Zhang, C. Chen, J. Zhang, G. Yang, L. Zheng, J. Zhang, B. Han, *Green Chem.* **2019**, *21*, 54.

[63] Z. Deng, H. Yu, L. Wang, J. Liu, K. J. Shea, *J. Mater. Chem. A* **2019**, *7*, 15975.

[64] Y. Zhou, Z. Li, Y. Liu, J. Huo, C. Chen, Q. Li, S. Niu, S. Wang, *ChemSusChem* **2020**, *13*, 1746.

[65] K. Titov, D. B. Eremin, A. S. Kashin, R. Boada, B. E. Souza, C. S. Kelley, M. D. Frogley, G. Cinque, D. Gianolio, G. Cibin, S. Rudić, V. P. Ananikov, J. C. Tan, *ACS Sustainable Chem. Eng.* **2019**, *7*, 5875.

[66] T. He, B. Ni, S. Zhang, Y. Gong, H. Wang, L. Gu, J. Zhuang, W. Hu, X. Wang, *Small* **2018**, *14*, e1703929.

[67] Z. W. Jiang, Y. C. Zou, T. T. Zhao, S. J. Zhen, Y. F. Li, C. Z. Huang, *Angew. Chem., Int. Ed.* **2020**, *621900*, 3300.

[68] Y. Wang, L. Feng, J. Pang, J. Li, N. Huang, G. S. Day, L. Cheng, H. F. Drake, Y. Wang, C. Lollar, J. Qin, Z. Gu, T. Lu, S. Yuan, H. C. Zhou, *Adv. Sci.* **2019**, *6*, 2.

[69] W. Shi, L. Cao, H. Zhang, X. Zhou, B. An, Z. Lin, R. Dai, J. Li, C. Wang, W. Lin, *Angew. Chem., Int. Ed.* **2017**, *56*, 9704.

[70] R. Xu, T. Drake, G. Lan, W. Lin, *Chem. – Eur. J.* **2018**, *24*, 15772.

[71] R. Xu, Z. Cai, G. Lan, W. Lin, *Inorg. Chem.* **2018**, *57*, 10489.

[72] G. Lan, Z. Li, S. S. Veroneau, Y.-Y. Zhu, Z. Xu, C. Wang, W. Lin, *J. Am. Chem. Soc.* **2018**, *140*, 12369.

[73] X. Hu, P. Chen, C. Zhang, Z. Wang, C. Wang, *Chem. Commun.* **2019**, *55*, 9657.

[74] G. Lan, Y. Quan, M. Wang, G. T. Nash, E. You, Y. Song, S. S. Veroneau, X. Jiang, W. Lin, *J. Am. Chem. Soc.* **2019**, *141*, 15767.

[75] Y. Quan, G. Lan, Y. Fan, W. Shi, E. You, W. Lin, Y. Quan, G. Lan, Y. Fan, W. Shi, E. You, W. Lin, *J. Am. Chem. Soc.* **2020**, *142*, 1746.

[76] H. Wang, L. Zhang, Z. Chen, J. Hu, S. Li, Z. Wang, J. Liu, X. Wang, *Chem. Soc. Rev.* **2014**, *43*, 5234.

[77] J. Ran, J. Qu, H. Zhang, T. Wen, H. Wang, S. Chen, L. Song, X. Zhang, L. Jing, R. Zheng, S.-Z. Qiao, *Adv. Energy Mater.* **2019**, *9*, 1803402.

[78] L. Chen, Y. Wang, F. Yu, X. Shen, C. Duan, *J. Mater. Chem. A* **2019**, *7*, 11355.

[79] L. Ye, Y. Gao, S. Cao, H. Chen, Y. Yao, J. Hou, L. Sun, *Appl. Catal., B* **2018**, *227*, 54.

[80] C. Zheng, X. Qiu, J. Han, Y. Wu, S. Liu, *ACS Appl. Mater. Interfaces* **2019**, *11*, 42243.

[81] D. Zhu, J. Liu, L. Wang, Y. Du, Y. Zheng, K. Davey, S. Z. Qiao, *Nanoscale* **2019**, *11*, 3599.

[82] Q. Hu, X. Huang, Z. Wang, G. Li, Z. Han, H. Yang, X. Ren, Q. Zhang, J. Liu, C. He, *J. Mater. Chem. A* **2020**, *8*, 2140.

[83] W. Zhang, Y. Wange, H. Zheng, R. Li, Y. Tang, C. Li, Z. Boyuan, L. You, M.-R. Gao, Z. Liu, S.-H. Yu, K. Zhou, *ACS Nano* **2020**, *14*, 1971.

[84] R. J. Li, Y. F. Qi, Q. Wang, J. J. Wang, Z. Y. Liu, X. G. Wang, X. J. Zhao, E. C. Yang, *J. Inorg. Gen. Chem.* **2020**, *646*, 1412.

[85] W. Cheng, X. F. Lu, D. Luan, X. W. Lou, *Angew. Chem., Int. Ed.* **2020**, *59*, 18234.

[86] C. Pan, Z. Liu, M. Huang, *Appl. Surf. Sci.* **2020**, *529*, 147201.

[87] S. W. Luo, R. Gu, P. Shi, J. Fan, Q. J. Xu, Y. L. Min, *J. Power Sources* **2020**, *448*, 227406.

[88] J. Huang, J.-Q. Wu, B. Shao, B.-L. Lan, F.-J. Yang, Y. Sun, X.-Q. Tan, C.-T. He, Z. Zhang, *ACS Sustainable Chem. Eng.* **2020**, *8*, 10554.

[89] P. Thangasamy, S. Shanmuganathan, V. Subramanian, *Nanoscale Adv.* **2020**, *2*, 2073.

[90] S. Zhao, Y. Wang, J. Dong, C. T. He, H. Yin, P. An, K. Zhao, X. Zhang, C. Gao, L. Zhang, J. Lv, J. Wang, J. Zhang, A. M. Khattak, N. A. Khan, Z. Wei, J. Zhang, S. Liu, H. Zhao, Z. Tang, *Nat. Energy* **2016**, *1*, 16184.

[91] W. Ye, Y. Yang, X. Fang, M. Arif, X. Chen, D. Yan, *ACS Sustainable Chem. Eng.* **2019**, *7*, 18085.

[92] J. Cui, J. Liu, C. Wang, F. Rong, L. He, Y. Song, Z. Zhang, S. Fang, *Electrochim. Acta* **2020**, *334*, 135577.

[93] M. Cai, Q. Liu, X. Zue, Y. Li, Y. Fan, A. Huang, M.-R. Li, M. Croft, T. A. Tyson, Z. Ke, G. Li, *J. Mater. Chem. A* **2020**, *8*, 190.

[94] W. Li, W. Fang, W. Chen, K. N. Dinh, H. Ren, L. Zhao, C. Liu, Q. Yan, *J. Mater. Chem. A* **2020**, *8*, 3658.

[95] L. Zhao, B. Dong, S. Li, L. Zhou, L. Lai, Z. Wang, S. Zhao, M. Han, K. Gao, M. Lu, X. Xie, B. Chen, Z. Liu, X. Wang, H. Zhang, H. Li, J. Liu, H. Zhang, X. Huang, W. Huang, *ACS Nano* **2017**, *11*, 5800.

[96] W. Pang, B. Shao, X.-Q. Tan, C. Tang, Z. Zhang, J. Huang, *Nanoscale* **2020**, *12*, 3623.

[97] R. Dong, M. Pfeffermann, H. Liang, Z. Zheng, X. Zhu, J. Zhang, X. Feng, *Angew. Chem., Int. Ed.* **2015**, *54*, 12058.

[98] R. Dong, Z. Zheng, D. C. Tranca, J. Zhang, N. Chandrasekhar, S. Liu, X. Zhuang, G. Seifert, X. Feng, *Chem. – Eur. J.* **2017**, *23*, 2255.

[99] Y. Song, Y. PI, X. Feng, K. Ni, Z. Xu, J. S. Chen, Z. Li, W. Lin, *J. Am. Chem. Soc.* **2020**, *142*, 6866.

[100] K. Rui, G. Zhao, M. Lao, P. Cui, X. Zheng, X. Zheng, J. Zhu, W. Huang, S. X. Dou, W. Sun, *Nano Lett.* **2019**, *19*, 8447.

[101] J.-X. Wu, S.-Z. Hou, X.-D. Zhang, M. Xu, H.-F. Yang, P.-S. Cao, Z.-Y. Gu, *Chem. Sci.* **2019**, *10*, 2199.

[102] X.-D. Zhang, S.-Z. Hou, J.-X. Wu, Z.-Y. Gu, *Chem. – Eur. J.* **2019**, *26*, 1604.

[103] Y. Guo, W. Shi, H. Yang, Q. He, Z. Zeng, J. Y. Ye, X. He, R. Huang, C. Wang, W. Lin, *J. Am. Chem. Soc.* **2019**, *141*, 17875.

[104] R. Al Natour, Z. K. Ali, A. Assoud, M. Hmadeh, *Inorg. Chem.* **2019**, *58*, 10912.

[105] J. Zha, X. Yin, J. R. Baltzegar, X. Zhang, *Langmuir* **2019**, *35*, 12908.

[106] D. J. Ashworth, A. Cooper, M. Trueman, R. W. M. Al-Saedi, S. D. Liam, A. J. Meijer, J. A. Foster, *Chem. – Eur. J.* **2018**, *24*, 17986.

[107] D. J. Ashworth, J. A. Foster, *Nanoscale* **2020**, *12*, 7986.

[108] C. X. Yu, F. L. Hu, J. G. Song, J. L. Zhang, S. S. Liu, B. X. Wang, H. Meng, L. L. Liu, L. F. Ma, *Sens. Actuators, B* **2020**, *310*, 127819.

[109] V. K. Maka, A. Mukhopadhyay, G. Savitha, J. N. Moorthy, *Nanoscale* **2018**, *10*, 22389.

[110] Y. H. Luo, C. Chen, C. He, Y. Y. Zhu, D. L. Hong, X. T. He, P. J. An, H. S. Wu, B. W. Sun, *ACS Appl. Mater. Interfaces* **2018**, *10*, 28860.

[111] A. K. Chaudhari, H. J. Kim, I. Han, J. C. Tan, *Adv. Mater.* **2017**, *29*, 1701463.

[112] G. Lan, K. Ni, E. You, M. Wang, A. Culbert, X. Jiang, W. Lin, *J. Am. Chem. Soc.* **2019**, *141*, 18964.

[113] W. Bai, S. Li, J. Ma, W. Cao, J. Zheng, *J. Mater. Chem. A* **2019**, *7*, 9086.

[114] J. Ma, W. Bai, J. Zheng, *Microchim. Acta* **2019**, *186*, 482.

[115] Y. Shu, J. Chen, Z. Xu, D. Jin, Q. Xu, X. Hu, *J. Electroanal. Chem.* **2019**, *845*, 137.

[116] D. Ning, Q. Liu, Q. Wang, X. M. Du, W. J. Ruan, Y. Li, *Sens. Actuators, B* **2019**, *282*, 443.

[117] H. Chen, Q. Qiu, S. Sharif, S. Ying, Y. Wang, Y. Ying, *ACS Appl. Mater. Interfaces* **2018**, *10*, 24108.

[118] J. Chen, Y. Shu, H. Li, Q. Xu, X. Hu, *Talanta* **2018**, *189*, 254.

[119] B. Tan, H. Zhao, W. Wu, X. Liu, Y. Zhang, X. Quan, *Nanoscale* **2017**, *9*, 18699.

[120] S. Hu, J. Yan, X. Huang, L. Guo, Z. Lin, F. Luo, B. Qiu, K. Y. Wong, G. Chen, *Sens. Actuators, B* **2018**, *267*, 312.

[121] M. Y. Shi, M. Xu, Z. Y. Gu, *Anal. Chim. Acta* **2019**, *1079*, 164.

[122] N. Zhu, L. Gu, J. Wang, X. Li, G. Liang, J. Zhou, Z. Zhang, *J. Phys. Chem. C* **2019**, *123*, 9388.

[123] T. M. Chen, X. J. Wu, J. X. Wang, G. W. Yang, *Nanoscale* **2017**, *9*, 11806.

[124] C. Wang, S. Huang, L. Luo, Y. Zhou, X. Lu, G. Zhang, H. Ye, J. Gu, F. Cao, *J. Electroanal. Chem.* **2019**, *835*, 178.

[125] S. S. Pan, W. Lu, Y. H. Zhao, W. Tong, M. Li, L. M. Jin, J. Y. Choi, F. Qi, S. G. Chen, L. F. Fei, S. F. Yu, *ACS Appl. Mater. Interfaces* **2013**, *5*, 12784.

[126] J. W. Zhang, H. T. Zhang, Z. Y. Du, X. Wang, S. H. Yu, H. L. Jiang, *Chem. Commun.* **2014**, *50*, 1092.

[127] L. Zhao, Y. Zhao, R. Li, D. Wu, X. Xie, H. Ye, Y. Zhang, Q. Xin, *Chem. Phys.* **2020**, *534*, 110743.

[128] M. Zhao, Y. Wang, Q. Ma, Y. Huang, X. Zhang, J. Ping, Z. Zhang, Q. Lu, Y. Yu, H. Xu, Y. Zhao, H. Zhang, *Adv. Mater.* **2015**, *27*, 7372.

[129] C. Liu, T. Wang, J. Ji, C. Wang, H. Wang, P. Jin, W. Zhou, J. Jiang, *J. Mater. Chem. C* **2019**, *7*, 10240.

[130] Q. Qiu, H. Chen, S. Ying, S. Sharif, Z. You, Y. Wang, Y. Ying, *Microchim. Acta* **2019**, *186*, 93.

[131] W.-J. J. Song, *Talanta* **2017**, *170*, 74.

[132] B. J. C. Wong, D. M. Xu, S. S. Bao, L. M. Zheng, J. Lei, *ACS Appl. Mater. Interfaces* **2019**, *11*, 12986.

[133] Q. Yang, J. Hong, Y.-X. Wu, Y. Cao, D. Wu, F. Hu, N. Gan, *ACS Appl. Mater. Interfaces* **2019**, *11*, 41506.

[134] H. S. Wang, J. Li, J. Y. Li, K. Wang, Y. Ding, X. H. Xia, *NPG Asia Mater* **2017**, *9*, e354.

[135] S. Wang, M. Wang, C. Li, H. Li, C. Ge, X. Zhang, Y. Jin, *Sens. Actuators, B* **2020**, *311*, 127919.

[136] L. Y. Yao, F. Yang, G. B. Hu, Y. Yang, W. Huang, W. B. Liang, R. Yuan, D. R. Xiao, *Biosens. Bioelectron.* **2020**, *155*, 112099.

[137] Y. Yang, G.-B. Hu, W.-B. Liang, L.-Y. Yao, W. Huang, Y.-J. Zhang, J.-L. Zhang, J.-M. Wang, R. Yuan, D.-R. Xiao, *Nanoscale* **2020**, *12*, 5932.

[138] M. Yan, J. Ye, Q. Zhu, L. Zhu, J. Huang, X. Yang, *Anal. Chem.* **2019**, *91*, 10156.

[139] G. B. Hu, C. Y. Xiong, W. B. Liang, Y. Yang, L. Y. Yao, W. Huang, W. Luo, R. Yuan, D. R. Xiao, *Biosens. Bioelectron.* **2019**, *135*, 95.

[140] L. Dong, L. Yin, G. Tian, Y. Wang, H. Pei, Q. Wu, W. Cheng, S. Ding, Q. Xia, *Sens. Actuators, B* **2020**, *308*, 127687.

[141] H. Xu, J. Gao, X. Qian, J. Wang, H. He, Y. Cui, Y. Yang, Z. Wang, G. Qian, *J. Mater. Chem. A* **2016**, *4*, 10900.

[142] L. J. Han, D. Zheng, S. G. Chen, H. G. Zheng, J. Ma, *Small* **2018**, *14*, 1703873.

[143] D. Liu, B. Liu, C. Wang, W. Jin, Q. Zha, G. Shi, D. Wang, X. Sang, *ACS Sustainable Chem. Eng.* **2020**, *8*, 2167.

[144] X. Qian, S. Deng, X. Chen, Q. Gao, Y. L. Hou, A. Wang, L. Chen, *Chin. Chem. Lett.* **2020**, *31*, 2211.

[145] G. Ding, Y. Wang, G. Zhang, K. Zhou, K. Zeng, Z. Li, Y. Zhou, C. Zhang, X. Chen, S. T. Han, *Adv. Funct. Mater.* **2019**, *29*, 1806637.

[146] M. G. Campbell, D. Sheberla, S. F. Liu, T. M. Swager, M. Dincǎ, *Angew. Chem., Int. Ed.* **2015**, *54*, 4349.

[147] M. D. Allendorf, A. Schwartzberg, V. Stavila, A. A. Talin, *Chem. – Eur. J.* **2011**, *17*, 11372.

[148] I. Stassen, N. Burtch, A. Talin, P. Falcaro, M. Allendorf, R. Ameloot, *Chem. Soc. Rev.* **2017**, *46*, 3185.

[149] M. Yuan, R. Wang, W. Fu, L. Lin, Z. Sun, X. Long, S. Zhang, C. Nan, G. Sun, H. Li, S. Ma, *ACS Appl. Mater. Interfaces* **2019**, *11*, 11403.

[150] J. F. Liao, W. Q. Wu, Y. Jiang, J. X. Zhong, L. Wang, D. B. Kuang, *Chem. Soc. Rev.* **2020**, *49*, 354.

[151] M. G. Campbell, S. F. Liu, T. M. Swager, M. Dincǎ, *J. Am. Chem. Soc.* **2015**, *137*, 13780.

[152] H. Liu, X. Li, L. Chen, X. Wang, H. Pan, X. Zhang, M. Zhao, *J. Phys. Chem. C* **2016**, *120*, 3846.

[153] Y. Shu, Y. Yan, J. Chen, Q. Xu, H. Pang, X. Hu, *ACS Appl. Mater. Interfaces* **2017**, *9*, 22342.

[154] Y. Zhao, L. Jiang, L. Shangguan, L. Mi, A. Liu, S. Liu, *J. Mater. Chem. A* **2018**, *6*, 2828.

[155] F. Su, S. Zhang, H. Ji, H. Zhao, J. Y. Tian, C. Sen Liu, Z. Zhang, S. Fang, X. Zhu, M. Du, *ACS Sens.* **2017**, *2*, 998.

[156] Y. Wang, M. Zhao, J. Ping, B. Chen, X. Cao, Y. Huang, C. Tan, Q. Ma, S. Wu, Y. Yu, Q. Lu, J. Chen, W. Zhao, Y. Ying, H. Zhang, *Adv. Mater.* **2016**, *28*, 4149.

[157] A. Pustovarenko, M. G. Goesten, S. Sachdeva, M. Shan, Z. Amghouz, Y. Belmabkhout, A. Dikhtiarenko, T. Rodenas, D. Keskin, I. K. Voets, B. M. Weckhuysen, M. Eddaoudi, L. C. P. M. de Smet, E. J. R. Sudhölter, F. Kapteijn, B. Seoane, J. Gascon, *Adv. Mater.* **2018**, *30*, 1707234.

[158] Y. Ning, X. Lou, C. Li, X. Hu, B. Hu, *Chem. – Eur. J.* **2017**, *23*, 15984.

[159] C. Li, X. Hu, W. Tong, W. Yan, X. Lou, M. Shen, B. Hu, *ACS Appl. Mater. Interfaces* **2017**, *9*, 29829.

[160] C. Shi, Y. Gao, L. Liu, Y. Song, X. Wang, H. J. Liu, Q. Liu, *J. Nanopart. Res.* **2016**, *18*, 3.

[161] C. Li, Q. Zhang, T. Li, B. He, P. Man, Z. Zhu, Z. Zhou, L. Wei, K. Zhang, G. Hong, Y. Yao, *J. Mater. Chem. A* **2020**, *8*, 3262.

[162] X. Zheng, Y. Cao, D. Liu, M. Cai, J. Ding, X. Liu, J. Wang, W. Hu, C. Zhong, *ACS Appl. Mater. Interfaces* **2019**, *11*, 15662.

[163] J. Yang, Z. Ma, W. Gao, M. Wei, *Chem. – Eur. J.* **2017**, *23*, 631.

[164] J. Wang, Q. Zhong, Y. Zeng, D. Cheng, Y. Xiong, Y. Bu, *J. Colloid Interface Sci.* **2019**, *555*, 42.

[165] H. M. Ma, J. W. Yi, S. Li, C. Jiang, J. H. Wei, Y. P. Wu, J. Zhao, D. S. Li, *Inorg. Chem.* **2019**, *58*, 9543.

[166] Y. Wang, Y. Liu, H. Wang, W. Liu, Y. Li, J. Zhang, H. Hou, J. Yang, *ACS Appl. Energy Mater.* **2019**, *2*, 2063.

[167] L. G. Beka, X. Bu, X. Li, X. Wang, C. Han, W. Liu, *RSC Adv.* **2019**, *9*, 36123.

[168] W. Zhao, W. Wang, J. Peng, T. Chen, B. Jin, S. Liu, W. Huang, Q. Zhao, *Dalton Trans.* **2019**, *48*, 9631.

[169] Y. Liu, Y. Wang, Y. Chen, C. Wang, L. Guo, *Appl. Surf. Sci.* **2020**, *507*, 145089.

[170] J. Xu, Y. Wang, S. Cao, J. Zhang, G. Zhang, H. Xue, Q. Xu, H. Pang, *J. Mater. Chem. A* **2018**, *6*, 17329.

[171] J. Cheng, S. Chen, D. Chen, L. Dong, J. Wang, T. Zhang, T. Jiao, B. Liu, H. Wang, J. J. Kai, D. Zhang, G. Zheng, L. Zhi, F. Kang, W. Zhang, *J. Mater. Chem. A* **2018**, *6*, 20254.

[172] S. Liu, Y.-C. Wang, C.-M. Chang, T. Yasuda, N. Fukui, H. Maeda, P. Long, K. Nakazato, W.-B. Jian, W. Xie, K. Tsukagoshi, H. Nishihara, *Nanoscale* **2020**, *12*, 6983.

[173] X. Hu, Z. Wang, B. Lin, C. Zhang, L. Cao, T. Wang, J. Zhang, C. Wang, W. Lin, *Chem. – Eur. J.* **2017**, *23*, 8390.

[174] W. Xing, P. Ye, J. Lu, X. Wu, Y. Chen, T. Zhu, A. Peng, H. Huang, *J. Power Sources* **2018**, *401*, 13.

[175] G. Li, R. Zhu, Y. Yang, *Nat. Photonics* **2012**, *6*, 153.

[176] P. Cheng, G. Li, X. Zhan, Y. Yang, *Nat. Photonics* **2018**, *12*, 131.

[177] C. Liu, C. Wang, H. Wang, T. Wang, J. Jiang, *Eur. J. Inorg. Chem.* **2019**, *2019*, 4815.

[178] K. Sasitharan, D. G. Bossanyi, N. Vaenas, A. J. Parnell, J. Clark, A. Iraqi, D. G. Lidzey, J. A. Foster, *J. Mater. Chem. A* **2020**, *8*, 6067.

[179] S. Wu, Z. Li, M. Li, Y. Diao, F. Lin, T. Liu, J. Zhang, P. Tieu, W. Gao, F. Qi, X. Pan, Z. Xu, Z. Zhu, A. K. Jen, *Nat. Nanotechnol.* **2020**, *15*, 934.

[180] M. G. Buonomenna, W. Yave, G. Golemme, *RSC Adv.* **2012**, *2*, 10745.

[181] J. Sánchez-Laínez, B. Zornoza, S. Friebe, J. Caro, S. Cao, A. Sabetghadam, B. Seoane, J. Gascon, F. Kapteijn, C. L. Guillouzer, G. Clet, M. Daturi, C. Téllez, J. Coronas, *J. Membr. Sci.* **2016**, *515*, 45.

[182] S. Japip, Y. Xiao, T. S. Chung, *Ind. Eng. Chem. Res.* **2016**, *55*, 9507.

[183] E. V. Perez, K. J. Balkus, J. P. Ferraris, I. H. Musselman, *J. Membr. Sci.* **2009**, *328*, 165.

[184] F. Yang, M. Wu, Y. Wang, S. Ashtiani, H. Jiang, *ACS Appl. Mater. Interfaces* **2019**, *11*, 990.

[185] Y. Peng, Y. Li, Y. Ban, W. Yang, *Angew. Chem., Int. Ed.* **2017**, *56*, 9757.

[186] Z. Kang, Y. Peng, Z. Hu, Y. Qian, C. Chi, L. Y. Yeo, L. Tee, D. Zhao, *J. Mater. Chem. A* **2015**, *3*, 20801.

[187] Y. Cheng, X. Wang, C. Jia, Y. Wang, L. Zhai, Q. Wang, D. Zhao, *J. Membr. Sci.* **2017**, *539*, 213.

[188] Y. Cheng, S. R. Tavares, C. M. Doherty, Y. Ying, E. Sarnello, G. Maurin, M. R. Hill, T. Li, D. Zhao, *ACS Appl. Mater. Interfaces* **2018**, *10*, 43095.

[189] M. Shete, P. Kumar, J. E. Bachman, X. Ma, Z. P. Smith, W. Xu, K. A. Mkhoyan, J. R. Long, M. Tsapatsis, *J. Membr. Sci.* **2018**, *549*, 312.

[190] Y. Yang, K. Goh, R. Wang, T. H. Bae, *Chem. Commun.* **2017**, *53*, 4254.

[191] M. Liu, K. Xie, M. D. Nothling, P. A. Gurr, S. S. L. Tan, Q. Fu, P. A. Webley, G. G. Qiao, *ACS Nano* **2018**, *12*, 11591.

[192] A. Sabetghadam, X. Liu, S. Gottmer, L. Chu, J. Gascon, F. Kapteijn, *J. Membr. Sci.* **2019**, *570–571*, 226.

[193] J. Deng, Z. Dai, J. Hou, L. Deng, *Chem. Mater.* **2020**, *32*, 4174.

**ADVANCED
SCIENCE NEWS**

www.advancedsciencenews.com

**ADVANCED
FUNCTIONAL
MATERIALS**

www.afm-journal.de

[194] Y. Peng, R. Yao, W. Yang, *Chem. Commun.* **2019**, *55*, 3935.

[195] R. Xu, M. Jian, Q. Ji, C. Hu, C. Tang, R. Liu, X. Zhang, J. Qu, *Chem. Eng. J.* **2020**, *382*, 122658.

[196] C. Wang, F. Liu, Z. Tan, Y. Chen, W. Hu, X. Xia, *Adv. Funct. Mater.* **2019**, *30*, 1908804.

[197] M. A. Shannon, P. W. Bohn, M. Elimelech, J. G. Georgiadis, B. J. Marĩas, A. M. Mayes, *Nature* **2008**, *452*, 301.

[198] B. Gao, Z. Jiang, M. Zhao, H. Wu, F. Pan, J. Q. Mayta, Z. Chang, X. Bu, *J. Membr. Sci.* **2018**, *546*, 31.

[199] J.-H. Deng, Y.-Q. Wen, J. Willman, W.-J. Liu, Y.-N. Gong, D.-C. Zhong, T.-B. Lu, H.-C. Zhou, *Inorg. Chem.* **2019**, *58*, 11020.

[200] R. Dai, X. Zhang, M. Liu, Z. Wu, Z. Wang, *J. Membr. Sci.* **2019**, *573*, 46.

[201] Z. Cao, V. Liu, A. B. Farimani, *Nano Lett.* **2019**, *19*, 8638.

[202] S. J. Tesh, T. B. Scott, *Adv. Mater.* **2014**, *26*, 6056.

[203] C. Wang, C. He, Y.-H. Luo, S. Su, J.-Y. Wang, D.-L. Hong, X.-T. He, C. Chen, B.-W. Sun, *Chem. Eng. J.* **2020**, *379*, 122337.

[204] S. Duan, L. Wu, J. Li, Y. Huang, X. Tan, T. Wen, T. Hayat, A. Alsaedi, X. Wang, *J. Hazard. Mater.* **2019**, *373*, 580.

[205] Y. Jiang, G. H. Ryu, S. H. Joo, X. Chen, S. H. Lee, X. Chen, M. Huang, X. Wu, D. Luo, Y. Huang, J. H. Lee, B. Wang, X. Zhang, S. K. Kwak, Z. Lee, R. S. Ruoff, *ACS Appl. Mater. Interfaces* **2017**, *9*, 28107.

[206] X. Zhao, Y. Wang, D. S. Li, X. Bu, P. Feng, *Adv. Mater.* **2018**, *30*, 1705189.

[207] P. Z. Moghadam, A. Li, X. W. Liu, R. Bueno-Perez, S. D. Wang, S. B. Wiggin, P. A. Wood, D. Fairen-Jimenez, *Chem. Sci.* **2020**, *11*, 8373.
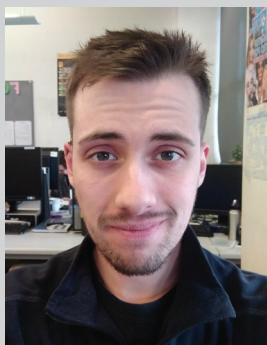
Joshua Nicks was awarded his MChem degree in 2017 from the University of Sheffield, under the supervision of Dr. Peter Portius. He is currently studying for his Ph.D. in chemistry at the same institution, under the supervision of Dr. Jonathan A. Foster. His research involves exploring the programmability of 2D metal-organic framework nanosheets and their applications.

Kezia Sasitharan completed her MSc in Chemistry at Christ University, India in 2017. She was awarded a Ph.D. in Chemistry in 2021 by The University of Sheffield, UK, under the supervision of Dr. Jonathan Foster. During her Ph.D. she researched the use of porphyrin MONs for enhanced performance of organic photovoltaic devices. She moved to Czech Technical University, Prague in 2021 after being awarded the Centre for Advanced Photovoltaics Postdoctoral Fellowship where she is currently exploring the role of low dimensional materials as additives for perovskite solar cells.

Ram R. R. Prasad obtained his master's from National Institute of Technology Trichy, where he completed a final year project under the guidance of Dr. S. Anandan. He went on to complete his Ph.D. at the University of St Andrews under the joint supervision of Prof. Paul Wright and Prof. Matt Clarke, where he investigated the use of metal-organic frameworks for tandem catalytic applications. Now in the Foster group, he is working on designing and functionalizing novel MONs for catalysis.

David J. Ashworth completed his MChem with study in industry at the University of Sheffield in 2016. He was awarded a Ph.D. in chemistry from the same institution in 2019 under the supervision of Dr. Jonathan Foster, researching the design and synthesis of functional MONs. He was then awarded an EPSRC Doctoral Prize Fellowship towards developing scalable routes of MON syntheses, in additional collaboration with Prof. Siddharth Patwardhan. Dave currently holds an EPSRC funded post-doctoral position at the University of Strathclyde, developing flexible, responsive MOFs with particular interest in gas adsorption properties.

Jonathan A. Foster completed his Ph.D. in the groups of Prof. Jonathan Steed and Prof. Judith Howard at the University of Durham before moving to the University of Cambridge with Prof. Jonathan Nitschke and Prof. Anthony Cheetham. In 2015 he was awarded a Ramsay Memorial Fellowship and the position of Vice Chancellors Fellow with the goal to develop metal-organic framework nanosheets (MONs) as a distinct class of 2D materials. He was appointed as lecturer in 2019 and his group continue to work with academic and industrial collaborators to develop MONs for a diverse range of applications.